Adaptive response of a metal–organic framework through reversible disorder–disorder transitions

S. Ehrling,[1] E. M. Reynolds,[2] V. Bon,[1] I. Senkovska,[1] T. E. Gorelik,[3] M. Rauche,[4] M. Mendt,[5] Manfred S. Weiss,[6] A. Pöppl,[5] E. Brunner,[4] U. Kaiser,[3] A. L. Goodwin*,[2] and S. Kaskel*,[1]

[1]Inorganic Chemistry Center I, Department of Chemistry, Technische Universität Dresden, Bergstr. 66, 01069, Dresden, Germany.

[2]Inorganic Chemistry Laboratory, Department of Chemistry, University of Oxford, South Parks Road, Oxford OX1 3QR, U.K.

[3]Electron Microscopy Group of Materials Science (EMMS), Central Facility for Electron Microscopy, Ulm University, Albert Einstein Allee 11, 89081 Ulm, Germany

[4]Chair of Bioanalytical Chemistry, Department of Chemistry, Technische Universität Dresden, Bergstr. 66, 01069, Dresden, Germany

[5]Felix Bloch Institute for Solid State Physics, Leipzig University, Linnéstr. 5, 04103, Leipzig, Germany

[6]Research Group Macromolecular Crystallography, Helmholtz-Zentrum Berlin für Materialien und Energie, Albert-Einstein-Straße 15, 12489 Berlin, Germany

*To whom correspondence should be addressed;
E-mail: andrew.goodwin@chem.ox.ac.uk or stefan.kaskel@tu-dresden.de.

A highly porous metal-organic framework (DUT-8(Ni), DUT = Dresden University of Technology) is found to adopt a configurationally-degenerate family of disordered states that respond adaptively to specific guest stimuli. This disorder originates from non-linear carboxylate linkers arranging paddle-wheels in closed loops of different local symmetries that in turn propagate as tilings of characteristic complex superstructures. Solvent exchange stimulates the formation of distinct disordered superstructures for specific guest molecules. Electron diffraction by desolvated DUT-8(Ni) nanoparticles demonstrates these superstructures to persist on the nanodomain level. Remarkably, guest exchange stimulates reversible and repeatable switching transitions between distinct disorder states. Deuterium NMR spectroscopy and *in situ* PXRD studies identify the transformation mechanism as an adaptive singular transformation event.

Introduction

Metal-Organic Frameworks (MOFs) have reached unexpected performance among other porous materials in terms of specific surface area, pore volume, functionality and structural variability.[1-5] These developments have resulted in a wide range of applications which are either commercialized or under investigation for applications in gas storage, separation, catalysis, sensing, electronics and many more.[6-8]

Flexibility is an important and appealing property exhibited by relatively few of the very many known MOFs.[9,10] In particular the ability to adapt the pore size to a guest molecule entering the pore system results in pronounced selectivity in gas separation[11-14], an almost ideal deliverable storage capacity[15-17] and novel enzyme-like responsivity of complex framework architectures.[18]

The very simplest prerequisite for flexibility is bistability, which allows switching between two distinguishable states in response to external stimuli. Canonical examples are the narrow and large pore states of breathing MOFs such as MIL-53[19] or DUT-49[20,21]. More complex behaviour emerges for systems with more than one accessible state. For example, the essentially continuous pore opening of MIL-88[22] and the induced-fit guest-recognition polymorphism of some hydrogen bonded frameworks[23] collectively identify the importance of more complex configurational landscapes for optimising catalytic or sensing architectures.

The sophisticated dynamic energy-landscape of these switchable MOFs motivated us to explore in detail the behaviour of a prototypical switchable model system, namely DUT-8(Ni) ([$Ni_2(2,6-ndc)_2dabco]_n$ (2,6-ndc = 2,6-naphthalenedicarboxylate, dabco = 1,4-diazabicyclo-(2,2,2)-octane). The basic structure of this MOF consists of paddle-wheels connected by 2,6-ndc linkers to form two-dimensional square (4,4) grids; axial coordination by dabco results in a highly porous pillared layer structure (Figure 1a,b). Despite its similarity to long-known analogues containing simple terephthalate linkers (DMOF[24]) and related systems, DUT-8(Ni) stands out demonstrating colossal stimuli-responsive switching transitions with up to 250% volume change induced by the adsorption of N_2 (77 K), CO_2 (195 K), Xe (165 K) alkanes and alkenes.[25,26] In-depth studies demonstrated not only the chemical composition[27,28] but also the particle size to massively affect the structural switching transition pressure.[29,30] DUT-8(Ni) is a highly selective adsorbent demonstrating solvent recognition phenomena and a guest-dependant pore opening mechanism.[31,32]

However, in our attempts to optimize synthesis conditions and single crystal growth we observed an unexpected variation of X-ray diffraction patterns - both single-crystal and powder - that precluded unambiguous assignment of symmetry and structure solution (Figure 1c,d) and suggested a surprising degree of polymorphism in this material. Parallel computational studies proposed such polymorphism might arise from different linker orientations, with severe implications on the switching mechanism.[33]
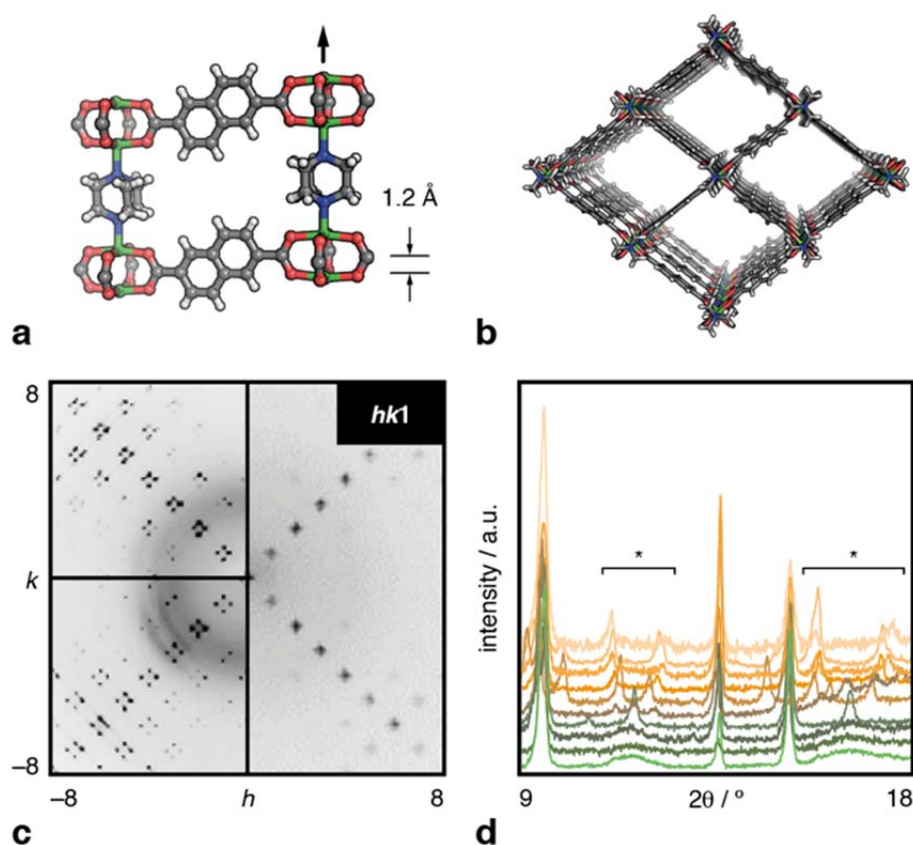

Figure 1. DUT-8 chemistry and anomalous diffraction behaviour. a Columns of dabco-linked Ni_2-paddle-wheels are displaced vertically with respect to their neighbours as a consequence of the step-like nature of the 2,6-ndc ligand. **b** Viewed down the column axis, the structure of DUT-8 is comprised of rhombic channels that, when fully open, are square in cross-section. **c** Single crystals of DUT-8 containing different guest species give surprisingly different and complex X-ray diffraction patterns that imply a variable domain-type substructure. **d** The same combination of variability and complexity is evident in powder X-ray diffraction measurements, particularly in those regions marked by an asterisk.

Here we demonstrate that DUT-8(Ni) is not polymorphic in the conventional sense, but rather adopts a degenerate family of disordered configurations. Remarkably, this configurational landscape can be navigated by guest sorption. This novel type of disorder-disorder switchability is fully reversible and multiple switching between distinct disorder variants is possible. X-ray and electron diffraction techniques in combination with solid state NMR and EPR studies provide insights into the microscopic switching mechanism.

Results

Discovery and rationalisation of disorder and structural diversity

In our initial attempts to understand the complex diffraction patterns observed experimentally, we carefully reconsidered all potential arrangements of the step-shaped linker and paddle-wheel (PW). The basic building block of the (4,4) net is a closed square loop, with paddle-wheel complexes as nodes (vertices) connected by 2,6-ndc (edges) (Figure 1). The higher level of complexity arises from the non-linearity of the linker (Figure 1a), representing an individual "stair" with a step-height of 1.2 Å in a complex 3D "staircase" (i.e. the framework). PWs connected by 2,6-ndc are not in the same plane but arranged in alternating heights. On proceeding around any given loop, there must be as many "up" steps as "down" steps (i.e. two of each) in order to satisfy its natural boundary conditions. There are exactly six possible up/down arrangements, four of which result in a loop with C_{2h} point symmetry and the other two give D_{2d} symmetry (Figure 2a, see also Supporting Information, Section 4).
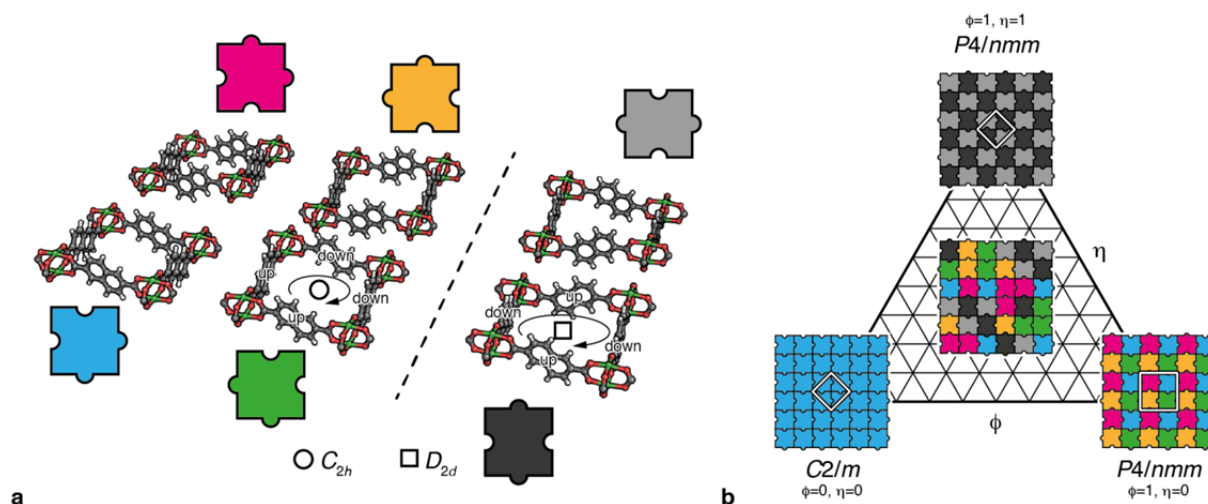
Figure 2. Models of disorder in DUT-8. a Representations of the six possible channel arrangements containing two "up" and two "down" 2,6-ndc orientations as the channel is traversed in a clockwise sense (circular arrows). These arrangements partition into two sets based on the point symmetry at the channel centre (circle and square). Each arrangement can be associated with a corresponding jigsaw tile. **b** The corresponding configurational landscape of valid jigsaw tilings, mapped in terms of the parameters ϕ and η described in the text. Limiting (ordered) configurations occupy the vertices of the triangular phase diagram (corresponding unit cells shown in white outline, and space-group symmetries given below); a representative disordered state is shown in the centre of the diagram.

Since neighbouring loops share edges, their corresponding states are not independent. The matching rules that emerge are captured by representing each loop by one of six "jigsaw" tiles (Figure 2a): any sensible jigsaw tiling corresponds to a physically sensible ensemble of 2,6-ndc orientations in the corresponding network structure.

A periodic concatenation of identically oriented (coloured) C_{2h} loops leads to an ordered tiling with monoclinic symmetry, earlier termed "polymorph B".[33] Likewise, the (greyscale) D_{2d} loops can also give an ordered tiling with tetragonal symmetry ("polymorph A").[33] However, our conceptual analysis reveals these two polymorphs to represent only two limiting, ordered instances of a much larger configurational landscape (Figure 2b). The statistical mechanics of the geometric model onto which our jigsaw tiling maps (the so-called "square-ice" model) is well understood, and the

system is known to support a finite configurational entropy.[34] In other words, the number of available DUT-8 configurations scales linearly with system size. This extensive configurational landscape contrasts the finite number of conformational states accessible even to protein-like hydrogen-bonded systems,[23] and also the continuous (but one-dimensional) spectrum of conformations in MIL-88 or SHF-61.[22,35] We identify specific DUT-8 states in terms of two parameters ϕ and η: the former represents the likelihood of neighbouring rows/columns adopting opposite 2,6-ndc orientations and the latter is simply the relative fraction of D_{2d} loops. Geometry dictates that $\phi \geq \eta$, since D_{2d} loops can only tile by alternating 2,6-ndc orientations.

Generating trial configurations and simulation of diffraction patterns

As the energetic landscape of correlated disordered states may severely impact the dynamic transformational behaviour and mechanical properties of the system it is essential to explain the unusual diffraction behaviour of DUT-8. We calculated PXRD patterns for a set of 55 structures in a 40 × 40 supercell of the parent DUT-8 framework structure covering a wide range of feasible configurations with varying ϕ,η values and compared them to our experimental powder diffraction data. We find that the surprising diversity of PXRD patterns observed experimentally is reflected also by the powder diffraction patterns calculated from our simplistic ϕ,η landscape. Then, by matching the PXRD traces of various solvent filled DUT-8 variants to our calculations, we can estimate the ϕ,η values that best describe their corresponding structures (Figure 3a,b). We note that the aim of this analysis is not to match quantitatively the observed peak intensities, since our structural models are intentionally simplistic (*e.g.* they do not contain guest molecules within pores).

Instead our focus is on establishing the extent to which the configurational landscape shown in Figure 2b can explain simultaneously the variety of peak broadening and splitting observed in some regions of the diffraction pattern and also the preservation of sharp features in other regions of the diffraction pattern.
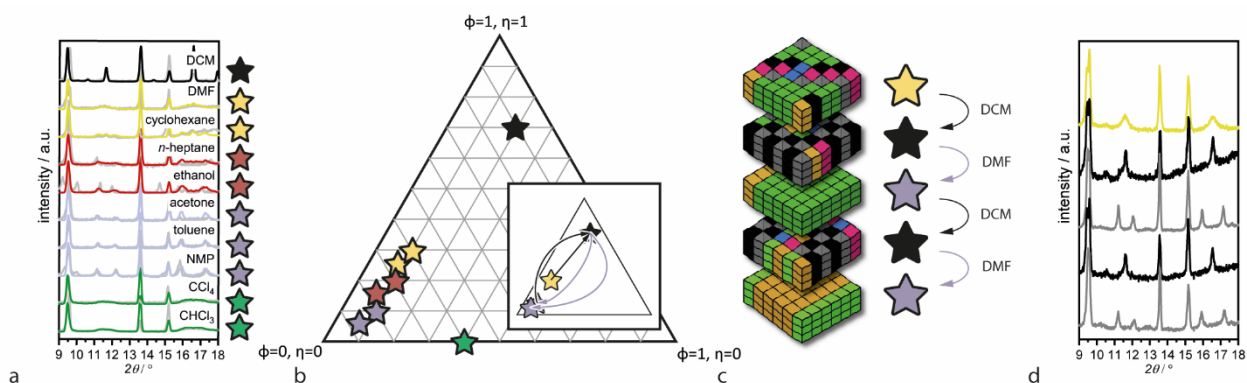

Figure 3. Experimental realisation of disordered DUT-8 states. a Comparison of experimental (grey lines) and best-fit calculated (coloured lines) powder X-ray diffraction patterns for DUT-8 samples loaded with a variety of different solvents. **b** Corresponding locations of each sample in configurational space. The inset shows the trajectory followed by a single sample during repeated guest exchange. **c** Representative configurations and **d** corresponding X-ray powder diffraction patterns associated with each step in this guest exchange process.

Not only do the as-synthesised frameworks (DMF, MeOH) correspond to disordered configurations (ϕ = 0.4, η = 0.3), but subsequent exchange with a wide range of solvents differing in size and polarity results in well-defined disordered configurations varying in ϕ and η (Figure 3b, Supporting Table S3). Amongst these, only the DCM-filled variant appears to contain a high fraction of D_{2d} loops (~70 %) while all other solvents investigated contain only 0–30 %. However, they differ markedly in ϕ (0.1-0.4) leading to pronounced differences in the experimental powder patterns (Figure 3a). The experimental evidence for these conclusions can be seen directly. For example, the reflections at 2θ = 10–13° appear particularly sensitive to 2,6-ndc orientations. Depending on these orientations, our PXRD patterns show either (i) a widening of the (111) peak, (ii) a splitting into (111) and (11-1) or (iii) a narrowing of

the (111) peak and an additional peak with low intensity at 10.5° (101). For example, *N*-methyl-2-pyrrolidone (NMP) and *n*-heptane induce the formation of a predominately monoclinic framework structure (ϕ = 0.1–0.3, η = 0.1-0.2). Samples immersed in chloroform and tetrachloromethane contain mixtures of type 1 loops (ϕ = 0.4, η = 0.0). Interestingly, only dichloromethane (DCM) induces linker orientations that correspond to an almost pure D_{2d} loop arrangement (ϕ = 0.9, η = 0.7). These findings are also supported by single crystal analyses. In the case of "as made" crystals (in DMF), tetragonal and monoclinic domains can be identified (Supporting Information, Section 3). However, single crystals filled with NMP or toluene in the pores show preferably monoclinic domains in the reciprocal space (Supporting Information, Figure S2) and resemble a four-component twin.

Electron diffraction and spectroscopic evidence of guest-controlled disorder

To clarify whether this characteristic disorder is truly persistent down to the nano-domain level and is not an artefact of our analysis we investigated DUT-8(Ni) nanocrystals via high resolution TEM and electron diffraction studies (Figure 4). Nanocrystals of DUT-8(Ni) are known to retain the open pore structure upon desolvation.[29,30] The persistence of a metastable *op*-phase has been termed a "shape memory effect" and is akin to a martensitic transformation.[28,36] High resolution TEM (Figure 4b) and electron diffraction studies of as made DUT-8(Ni) nanocrystals reveal whether distinct disorder patterns persist at nanodomain level (Figure 4c). Note that the simultaneous presence of both tetragonal (labelled '2') and monoclinic (labelled '1,3') reflections in the single diffraction pattern of Figure 4c implies the coexistence of multiple domains within a single nanocrystallite. Inverse Fourier transformation (FT) analysis of the power spectra allow localisation of the

corresponding domains in real-space. The presence of diffuse reflections is a clear indication for stacking faults in the structure. The deconvolution of diffuse reflections into several regions in *c* direction (as shown in projection in Figure 4d-f) demonstrates the simultaneous presence of nanodomains with tetragonal and monoclinic structure within one nanocrystal. This observation provides strong evidence that the interpretation of diffraction data based on the disorder model outlined above is reasonable.
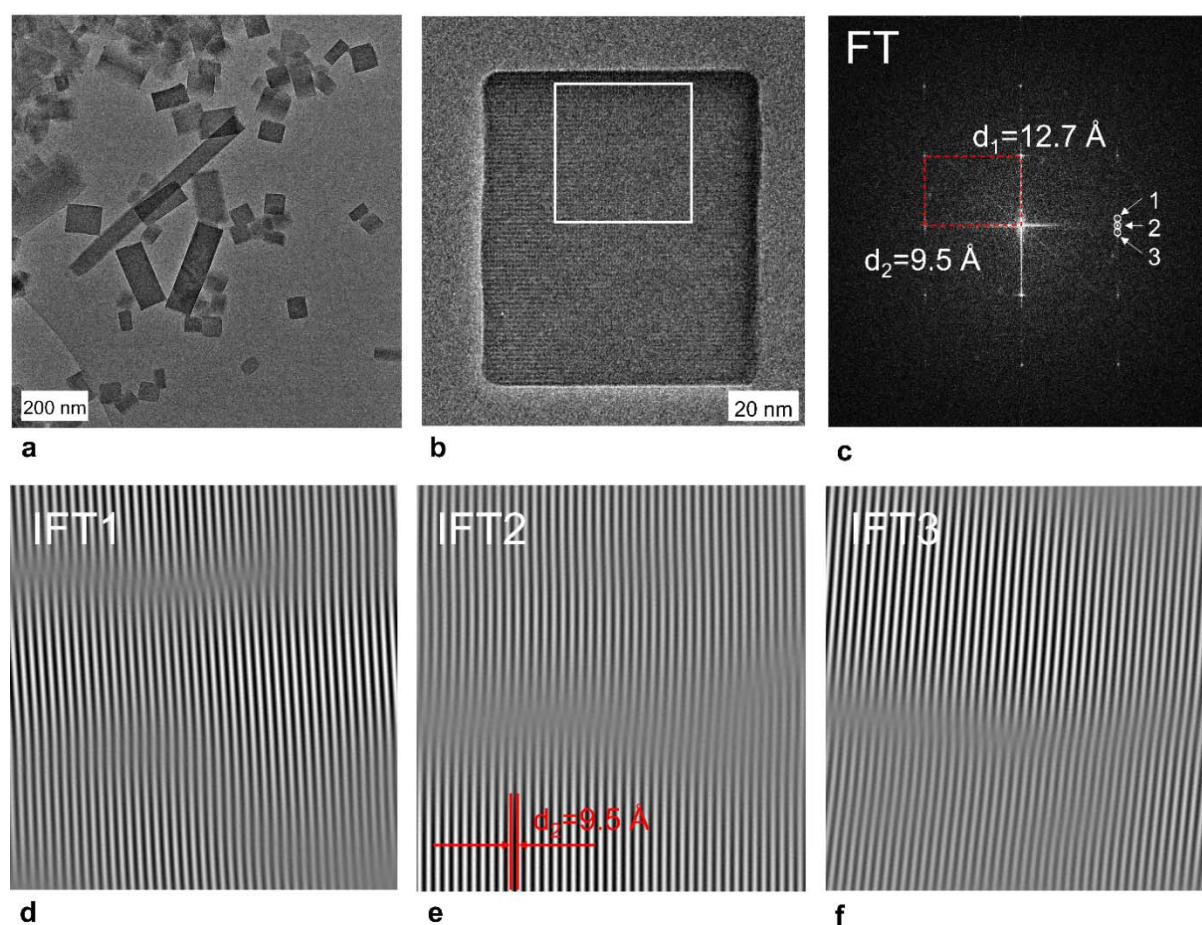

Figure 4. Electron microscopy analysis of disordered DUT-8(Ni) nanocrystals. **a** An overview TEM image. **b** High-resolution TEM image, and **c** corresponding power spectrum (Fourier transformation) of the marked area. The HR image shows a crystal along [110]; the corresponding power spectrum contains reflections with the interplanar distances of 12.7 Å (characteristic PW–ndc–PW separation) and 9.5 Å (characteristic PW–dabco–PW separation). Diffuse scattering along the c^* direction is evident. **d-f** The inverse Fourier transformation (IFT) analysis of the power spectra was performed using different positions of diffuse streak (1 - 3) shown in **c**. IFT area corresponds to the rectangular region marked in **b**. High-contrast patches in IFT patterns correspond to the crystal areas with the selected lattice fringes.

It should be emphasized that these disordered configurations imply the presence of four local PW configurations differing in local symmetry due to the relative arrangement of the surrounding "stairs" (Supporting Information, Section 4, Figure S5b). These local configurations imply differences in continuous wave electron paramagnetic resonance (EPR) spectra through distinct variations of the local symmetry. Through deliberate doping, we introduce a spectator probe ion (Co^{2+}) into DUT-8(Ni) in low concentration of DUT-8($Ni_{0.98}Co_{0.02}$) (Supporting Information, Section 9). The incorporation of an EPR visible d^7-probe in mixed-metal Ni^{2+}-Co^{2+} paddle-wheel units of the *op*-phase provides a *high spin* Co^{2+} ion ($S = 3/2$) coupling magnetically with a *high spin* Ni^{2+} ($S = 1$) to form a state with a total effective electron spin $S = 1/2$. Due to the hyperfine interaction (*hfi*) with the ^{59}Co nucleus ($I = 7/2$) evaluation of the sample specific g- and hyperfine interaction tensors gives insights into the local paddle-wheel configuration. For the DCM loaded samples, the *x* and *y* principal values of the g- and *hfi*-tensors are close to each other, indicating a high degree of axial symmetry and suggesting that the corresponding paddle-wheel units have an essentially fourfold rotational symmetry axis as expected for a high fraction of D_{2d} loops. However, for the DMF and *n*-heptane solvated samples the dominating 2,6-ndc coordination to the paddle-wheels shows no fourfold symmetry axis. These spectroscopic signatures are in good agreement with the crystallographic analysis and disorder models developed.

Discussion

To the best of our knowledge this is the first report of guest-driven configuration control in distinctly disordered superstructures of a highly flexible MOF. Obviously, the host–guest interaction subtly directs the framework through energetic

stabilization into a new disordered configuration – essentially an adaptive molecular response in the ϕ,η landscape promoting a characteristic distribution of loops. It is beyond the scope of our study (and likely also the capability of current simulation methodologies) to explore rigorously the specifics of these solvent–host interactions. However, it is chemically intuitive that differences in adsorption enthalpy and solvent packing will likely affect the structural equilibrium of the interacting host–guest system for different guests. In this context it is interesting to note the singular role of DCM which has a high adsorption enthalpy ($|\Delta_{ads}H| = 35 - 50 \; kJ \; mol^{-1}$)[28] and dipole moment (1.8 D).[37]

Recently switchability in frameworks has led to the discovery of unexpected novel phenomena such as negative gas adsorption (NGA).[20,21,38,39] Switchability is a unique characteristic of a chosen few MOFs with the ability to adapt their pore size dynamically leading to extra-high selectivity in gas separation, ideal deliverable storage capacity in natural gas storage as well as promising sensing and catalytic functionality.[6-8,11-18,40] Hence, we were curious if switching between well-defined disordered configurations is achievable simply by repeated guest exchange.

By selecting two solvents resulting in markedly distinct powder patterns, namely DCM and DMF, we could indeed observe fully reversible switching between two disordered states (Figure 3c,d). The switching is easily discerned by following the evolution of the characteristic region (2θ = 10-14°) of the X-ray diffraction pattern demonstrating reversible switching between a configuration high in D_{2d} (DCM) and a predominately monoclinic one (DMF). Time-resolved studies indicate a complete conversion from one state into the other over ~30 minutes. Hence the configurational landscape of Figure 2b is at least partially navigable by suitable guest exchange chemistry.

Disorder-disorder switching may result either from (i) concerted rotation of 2,6-ndc linkers converting steps from up to down, associated with correlated translations of PW–dabco columns and microdomain boundaries moving through the crystal, or (ii) a dissolution–nucleation mechanism. The latter would imply that non-solvents for framework components, such as *n*-heptane, would suppress such a reversible transformation. This is clearly not the case. Hence navigation of the DUT-8(Ni) configurational landscape proceeds – remarkably – via concerted vertical translations of linear columns of alternating paddle-wheel and dabco units shifting up and down, "*en bloc*", throughout entire crystallites.

For an understanding of this movement it is important to clarify whether the 2,6-ndc linkers are permanently rotating in the solvated state, thermally activated pushing the paddle-wheel columns up and down, or the transformation is a single event induced by a specific solvent–framework interaction. To answer this question, we recorded solid state NMR spectra of DUT-8(Ni) containing deuterated 2,6-ndc linkers in order to analyse the rotational mobility of the 2,6-ndc linker in equilibrium after solvent exchange (Figure 5). ^{2}H NMR spectroscopy is a powerful tool for studying dynamic properties of solids.[41-44] The electric quadrupole interactions of the spins (I=1) dominate the spectra. Typically, the electric field gradient tensor for deuterons in C-D bonds is nearly axially symmetric[41], which is advantageous to observe molecular motions as well as the orientational distribution in the presence of partial ordering.[44] Various types of fast motion can be distinguished by evaluating characteristic line shapes of the ^{2}H spectra. Static deuteron NMR spectra of solids are very broad and typically cover a frequency range up to 250 kHz.[43] To excite such a large frequency range and enhance the signal to noise ratio wide-line techniques like the WURST (wideband uniform-rate smooth truncation) pulse sequence combined with CPMG

(Carr-Purcell Meiboom-Gill) pulse sequence were used.[45] In the given case of Pake doublets (Figure 5), the distance between both intensity maxima (further denoted as peak separation) depends on fast motions of the linker molecules.[46]

In Figure 5a, the peak separation is about 125 kHz, a typical value for immobile C-D groups, irrespective of the guests. Hence, the 2,6-ndc linkers do not perform thermally activated fast 180° flips irrespective of the solvent. Only DUT-8(Ni) loaded with DMF shows an additional signal in the middle of the spectrum with ca. 16 kHz line width. This small line width indicates a fast motion of a small fraction of the linkers, possibly indicating rotation of free linker on the surface.

To also enable the detection of possible slow motions, we measured 2D EXSY (exchange spectroscopy) experiments on deuterated DUT-8(Ni). Comparison of calculated line shapes (Figure 5b) for various motions with experimental data in Figure 5c indicates that the linker is immobile up to the time scale of hundreds of millioseconds corresponding to rates of several Hertz. Over the temperature range 243-343 K, there is no change in the ^{2}H NMR spectra visible. This indicates that temperature increase has no noticeable influence on linker mobility.
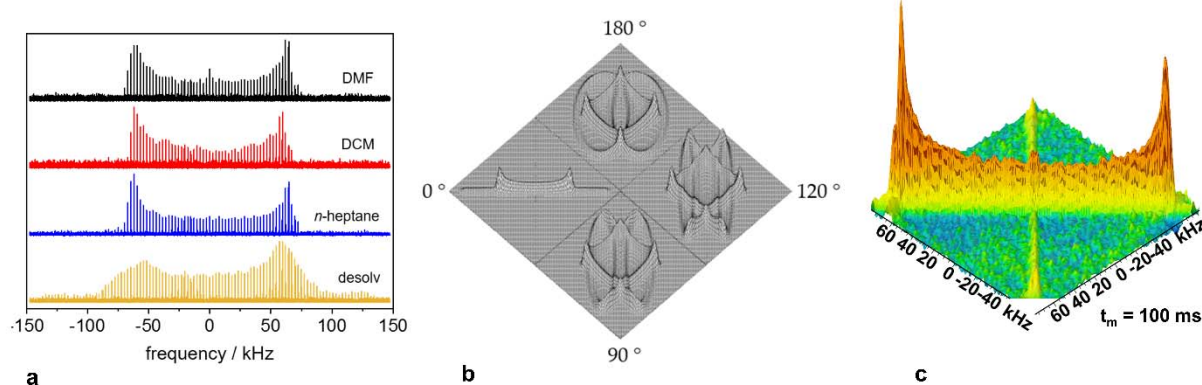

Figure 5. NMR results. a WURST Q-CPMG ^{2}H NMR Spectra of DUT-8(Ni) loaded with different solvents and solvent free (desolv). **b** Calculated 2D EXSY spectra for possible molecular dynamics (calculations were performed for linker flips with the indicated flip angles using WEBLAB[47]) and **c** 2D EXSY NMR experiment for DUT-8(Ni) solvated with DMF measured for a mixing time t_m of 100 ms.

Consequently, our ^{2}H NMR measurements indicate that the majority (99 %) of the linkers are interlocked after solvation and only a low concentration of freely-rotating linkers is detected with little variation for varying solvents. From this observation, a free thermally-activated rotation of the linker in the solvated framework at room temperature can be ruled out. Instead, each solvent locks the framework in a specific disordered superstructure configuration in the ϕ,η landscape. It is only by introducing a new guest that one stimulates the concerted reorientation of the framework constituents at once.

The disordered nature of DUT-8(Ni) has also profound implications for its dynamic pore closing mechanism. By analysing the pore closing dynamics of three prototypical cases representing a predominately tetragonal (DCM) vs. a monoclinic (*n*-heptane) domain architecture, and an intermediate case (DMF) we find monoclinic domains to directly close their pores while tetragonal domains containing D_{2d} loops to rotate linker orientations leading to C_{2h} loops (monoclinic domains) before pore closing into the *cp*-phase of DUT-8(Ni) (Supporting Information, Section 8, Figure S12). This observation implies significant differences in the transformation mechanisms and trajectories of dynamic networks depending on their disorder configuration and may offer a strategy to tune the activation barriers and associated kinetics of adaptive pore structure transformations in future.

Summarizing, we have uncovered a new type of responsive behaviour in open frameworks involving interconversion between meaningfully-different disordered states. It is the specific type of symmetry lowering associated with stair-shaped framework components such as 2,6-ndc, that when combined with the underlying square lattice of the DUT-8(Ni) structure leads to an extensive configurational landscape. Host–guest interactions perturb the energetics of this landscape such

that the system responds adaptively to guest adsorption. Repeated solvent exchange demonstrates reversible switching between distinct disordered states. This new type of framework disorder-disorder switchability demonstrates a quasi-continuous dynamic transformation from one state into another. Each guest species encodes a complex microdomain structure (tiling) in the framework crystal recording the exposure history and molecular information in the material. The complex disorder pattern stores this type of information through the crystalline framework architecture.[48] Given the multitude of non-linear linkers employed for the design of MOFs, COFs and more recently 2D materials we conceive disorder-disorder switchability to be of wider importance for framework materials than hitherto expected. Moreover, the control of disordered configurations may pave a new way to encode open frameworks with complex information and consequently distinct implications for their physical characteristics such as optical, magnetic and micromechanics.[48] In particular the activation energy and transformation rate of adaptive pore closing and opening phenomena are expected to become history dependent with important implications for the application of switchable MOFs in gas separation, storage and sensing devices.

Methods

Detailed information on the synthesis of materials, instrumental parameters and conditions for diffraction and spectroscopic analysis, disorder models, single crystal X-ray diffraction, HR TEM, simulated ^{2}H NMR spectra, and EPR spectra are described in the Supporting Information.

Data availability: The data supporting the findings of this study are available within the article and the supplementary materials. The corresponding raw data are available from the corresponding author. Single crystal structures can be obtained free of charge from the Cambridge Crystallographic Data Centre via www.ccdc.cam.ac.uk/data_request/cif. CCDC-1989709 and CCDC-1989708 contain the supplementary crystallographic data for DMF@DUT-8(Ni) of polymorph A and DUT-8(Ni) polymorph B, respectively. CCDC- 1989557-1989560 contain the supplementary crystallographic data for NMP@DUT-8(Ni) and toluene@DUT-8(Ni), respectively. For each solvent two independent refinements are provided considering a single domain crystal or a four-component twin as explained in the supplementary information.

References

1   Hönicke, I. M. *et al.* Balancing mechanical stability and ultrahigh porosity in crystalline framework materials. *Angew. Chem. Int. Ed.* **57**, 13780-13783 (2018).

2   Maurin, G., Serre, C., Cooper, A. & Férey, G. The new age of MOFs and of their porous-related solids. *Chem. Soc. Rev.* **46**, 3104-3107 (2017).

3   Huang, Y.-B., Liang, J., Wang, X.-S. & Cao, R. Multifunctional metal–organic framework catalysts: synergistic catalysis and tandem reactions. *Chem. Soc. Rev.* **46**, 126-157 (2017).

4   Zhou, H.-C., Long, J. R. & Yaghi, O. M. Introduction to metal–organic frameworks. *Chem. Rev.* **112**, 673-674 (2012).

5   Stock, N. & Biswas, S. Synthesis of metal-organic frameworks (MOFs): routes to various MOF topologies, morphologies, and composites. *Chem. Rev.* **112**, 933-969 (2011).

6   Caro, J. Quo vadis, MOF? *Chem. Ing. Tech.* **90**, 1759-1768 (2018).

7   Fathieh, F. *et al.* Practical water production from desert air. *Sci. Adv.* **4**, eaat3198 (2018).

8   Chen, Y. *et al.* Stabilization of formate dehydrogenase in a metal–organic framework for bioelectrocatalytic reduction of CO_2. *Angew. Chem. Int. Ed.* **58**, 7682 (2019).

9   Schneemann, A. *et al.* Flexible metal–organic frameworks. *Chem. Soc. Rev.* **43**, 6062-6096 (2014).

10   Lee, J. H., Jeoung, S., Chung, Y. G. & Moon, H. R. Elucidation of flexible metal-organic frameworks: research progresses and recent developments. *Coord. Chem. Rev.* **389**, 161-188 (2019).

11   Yang, S. *et al.* A partially interpenetrated metal–organic framework for selective hysteretic sorption of carbon dioxide. *Nat. Mater.* **11**, 710 (2012).

12   Duan, J. *et al.* High $CO_2/N_2/O_2/CO$ separation in a chemically robust porous coordination polymer with low binding energy. *Chem. Sci.* **5**, 660-666 (2014).

13   Li, L. *et al.* Efficient separation of ethylene from acetylene/ethylene mixtures by a flexible-robust metal–organic framework. *J. Mater. Chem. A* **5**, 18984-18988 (2017).

14   Taylor, M. K. *et al.* Near-Perfect CO_2/CH_4 selectivity achieved through reversible guest templating in the flexible metal–organic framework Co(bdp). *J. Am. Chem. Soc.* **140**, 10324-10331 (2018).

15   Mason, J. A. *et al.* Methane storage in flexible metal–organic frameworks with intrinsic thermal management. *Nature* **527**, 357 (2015).

16   Li, H. *et al.* Recent advances in gas storage and separation using metal–organic frameworks. *Mater. Today* **21**, 108-121 (2018).

17   Kundu, T., Wahiduzzaman, M., Shah, B. B., Maurin, G. & Zhao, D. Solvent-induced control over breathing behavior in flexible metal–organic frameworks for natural-gas delivery. *Angew. Chem. Int. Ed.* **58**, 8073–8077 (2019).

18   Katsoulidis, A. P. *et al.* Chemical control of structure and guest uptake by a conformationally mobile porous material. *Nature* **565**, 213 (2019).

19   Serre, C. *et al.* Very large breathing effect in the first nanoporous chromium(III)-based solids: MIL-53 or $Cr^{III}(OH)\{O_2C-C_6H_4-CO_2\}\{HO_2C-C_6H_4-CO_2H\}_xH_2O_y$. *J. Am. Chem. Soc.* **124**, 13519-13526 (2002).

20   Krause, S. *et al.* A pressure-amplifying framework material with negative gas adsorption transitions. *Nature* **532**, 348 (2016).

21   Krause, S. *et al.* Towards general network architecture design criteria for negative gas adsorption transitions in ultraporous frameworks. *Nat. Commun.* **10**, 1-12 (2019).

22   Serre, C. *et al.* Role of solvent-host interactions that lead to very large swelling of hybrid frameworks. *Science* **315**, 1828-1831 (2007).

23   Katsoulidis, A. P. *et al.* Chemical control of structure and guest uptake by a conformationally mobile porous material. *Nature* **565**, 213-217 (2019).

24   Dybtsev, D. N., Chun, H. & Kim, K. Rigid and flexible: a highly porous metal–organic framework with unusual guest-dependent dynamic behavior. *Angew. Chem. Int. Ed.* **43**, 5033-5036 (2004).

25   Bon, V. *et al.* Exceptional adsorption-induced cluster and network deformation in the flexible metal–organic framework DUT-8(Ni) observed by in situ X-ray diffraction and EXAFS. *Phys. Chem. Chem. Phys.* **17**, 17471-17479 (2015).

26   Klein, N. *et al.* Monitoring adsorption-induced switching by [129]Xe NMR spectroscopy in a new metal–organic framework $Ni_2(2,6-ndc)_2(dabco)$. *Phys. Chem. Chem. Phys.* **12**, 11778-11784 (2010).

27   Klein, N. *et al.* Structural flexibility and intrinsic dynamics in the $M_2(2,6-ndc)_2(dabco)$(M= Ni, Cu, Co, Zn) metal–organic frameworks. *J. Mater. Chem.* **22**, 10303-10312 (2012).

28   Ehrling, S. *et al.* Crystal size versus paddle wheel deformability: selective gated adsorption transitions of the switchable metal-organic frameworks DUT-8(Co) and DUT-8(Ni). *J. Mater. Chem. A* **7**, 21459-21475 (2019).

29   Kavoosi, N. *et al.* Tailoring adsorption induced phase transitions in the pillared-layer type metal–organic framework DUT-8(Ni). *Dalton Trans.* **46**, 4685-4695 (2017).

30   Miura, H. *et al.* Tuning the gate-opening pressure and particle size distribution of the switchable metal–organic framework DUT-8(Ni) by controlled nucleation in a micromixer. *Dalton Trans.* **46**, 14002-14011 (2017).

31   Kavoosi, N. *et al.* Selective pore opening and gating of the pillared layer metal-organic framework DUT-8(Ni) upon liquid phase multi-component adsorption. *Microporous Mesoporous Mater.* **271**, 169-174 (2018).

32   Rauche, M. *et al.* New insights into solvent-induced structural changes of ^{13}C labelled metal-organic frameworks by solid state NMR. *Chem. Commun.* **55**, 9040 (2019).

33   Petkov, P. S. *et al.* Conformational isomerism controls collective flexibility in metal–organic framework DUT-8(Ni). *Phys. Chem. Chem. Phys.* **21**, 674-680 (2019).

34   Lieb, E. H. Residual entropy of square ice. *Phys. Rev.* **162**, 162 (1967).

35   Carrington, E. J. *et al.* Solvent-switchable continuous-breathing behaviour in a diamondoid metal–organic framework and its influence on CO_2 versus CH_4 selectivity. *Nat. Chem.* **9**, 882 (2017).

36   Sakata, Y. *et al.* Shape-memory nanopores induced in coordination frameworks by crystal downsizing. *Science* **339**, 193-196 (2013).

37   Smallwood, I. *Handbook of organic solvent properties* (Butterworth-Heinemann, 2012).

38   Krause, S. *et al.* The effect of crystallite size on pressure amplification in switchable porous solids. *Nat. Commun.* **9**, 1573 (2018).

39   Kolbe, F. *et al.* High pressure in situ ^{129}Xe NMR spectroscopy: insights into switching mechanisms of flexible metal-organic frameworks isoreticular to DUT-49. *Chem. Mater.* **31**, 6193-6201 (2019).

40   Yuan, S. *et al.* Flexible zirconium metal-organic frameworks as bioinspired switchable catalysts. *Angew. Chem. Int. Ed.* **55**, 10776-10780 (2016).

41   Barnes, R., Torgeson, D. & Bray, P. On NMR powder spectrum simulation for nuclei with I>1/2. *Phys. Status Solidi B* **147**, K175-K178 (1988).

42   Schmidt-Rohr, K. & Spiess, H. W. *Multidimensional solid-state NMR and polymers* (Elsevier, 2012).

43   Spiess, H. W. Molecular dynamics of solid polymers as revealed by deuteron NMR. *Colloid. Polym. Sci.* **261**, 193-209 (1983).

44   Spiess, H. W. & Sillescu, H. Solid echoes in the slow-motion region. *J. Magn. Reson.* **42**, 381-389 (1981).

45   O'Dell, L. A. & Schurko, R. W. QCPMG using adiabatic pulses for faster acquisition of ultra-wideline NMR spectra. *Chem. Phys. Lett.* **464**, 97-102 (2008).

46   Duer, M. J. *Introduction to solid-state NMR spectroscopy* (Wiley-Blackwell, 2005).

47   Macho, V., Brombacher, L., Graf, R. & Spiess, H. W. *NMR WEBLAB*, MPI for Polymer Research, Mainz, https://weblab2.mpip-mainz.mpg.de/weblab66/ (2018).

48   Simonov, A. & Goodwin, A. L. Designing disorder into crystalline materials. *Prepint at https://www.arxiv-vanity.com/papers/1912.00366/* (2019).

Acknowledgements

Author contributions

S. Ehrling and V. Bon synthesized and characterized all materials by X-ray diffraction. M. S. Weiss supported the collection of single crystal X-ray data. E. Reynolds and A. L. Goodwin developed the disorder models. I. Senkovska, T. E. Gorelik and U. Kaiser analyzed the domain structure of nanocrystals based on TEM and electron diffraction data. M. Rauche and E. Brunner performed and interpreted the ^{2}H NMR spectra. M. Mendt and A. Pöppl measured and interpreted the EPR spectra. A. L. Goodwin and S. Kaskel initiated and conceptually coordinated the study. All authors contributed to writing and improving the manuscript.

Competing interests

The authors declare no competing interests.

Supporting Information

Adaptive response of a metal–organic framework through reversible disorder–disorder transitions

S. Ehrling,[1] E. M. Reynolds,[2] V. Bon,[1] I. Senkovska,[1] T. E. Gorelik,[3] M. Rauche,[4] M. Mendt,[5] Manfred S. Weiss,[6] A. Pöppl,[5] E. Brunner,[4] U. Kaiser,[3] A. L. Goodwin*,[2] and S. Kaskel*,[1]

[1]Inorganic Chemistry Center I, Department of Chemistry, Technische Universität Dresden, Bergstr. 66, 01069, Dresden, Germany.

[2]Inorganic Chemistry Laboratory, Department of Chemistry, University of Oxford, South Parks Road, Oxford OX1 3QR, U.K.

[3]Electron Microscopy Group of Materials Science (EMMS), Central Facility for Electron Microscopy, Ulm University, Albert Einstein Allee 11, 89081 Ulm, Germany.

[4]Bioanalytical Chemistry Laboratory, Department of Chemistry, Technische Universität Dresden, Bergstr. 66, 01069, Dresden, Germany.

[5]Felix Bloch Institute for Solid State Physics, Leipzig University, Linnéstr. 5, 04103, Leipzig, Germany.

[6]Research Group Macromolecular Crystallography, Helmholtz-Zentrum Berlin für Materialien und Energie, Albert-Einstein-Straße 15, 12489 Berlin, Germany.

Table of contents

1 Materials and syntheses

1.1 Chemicals

Ni(NO$_3$)$_2$·6H$_2$O (≥ 98%), Co(NO$_3$)$_2$·6H$_2$O (≥ 98%), 2,6-H$_2$ndc (99%), dabco were purchased from Sigma Aldrich. 2,6-Naphthalenedicarboxylic-d6 acid (d6-H$_2$ndc, deuterium content > 98%) was purchased from CDN ISOTOPES.

All solvents were at least of analytical grade, purchased from commercial suppliers and used without further purification. Detailed information is given in table S1.

Table S1. Specification of the used solvents.

Solvent	Purity	Purchased from
Acetone	≥ 99.5%	ALFA AESAR
Chloroform	99%	SIGMA-ALDRICH
Cyclohexane	99.98%	FISCHER
Dichloromethane	≥ 99.8 %	SIGMA-ALDRICH
Ethanol	HPLC grade	FISCHER
N,N-Dimethylformamide	99.5%	SIGMA-ALDRICH
n-Heptane	97%	SIGMA-ALDRICH
N-Methyl-2-pyrrolidone	99%	ACROS
Tetrachloromethane	99%	SIGMA-ALDRICH
Toluene	99.7%	SIGMA-ALDRICH

1.2 Synthesis of DUT-8(Ni)

The synthesis procedure was adapted from KAVOOSI *et al.*[1] Typically, Ni(NO$_3$)$_2$·6H$_2$O (404 mg, 1.4 mmol, 1.56 äq.) is dissolved in 6 mL DMF, 2,6-H$_2$ndc (303 mg, 1.4 mmol, 1.56 äq.) is dissolved in 15 mL DMF, and dabco (100 mg, 0.9 mmol) is dissolved in 9 mL MeOH. The resulting solutions are combined, transferred into a Teflon inlet, heated in an autoclave to 120 °C and annealed for 48 hours. After cooling down, the supernatant reaction solution is removed by decantation and the dark green crystals are washed with fresh DMF several times.

1.3 Synthesis of DUT-8(Ni) nanoparticles

The synthesis procedure was adapted from KAVOOSI *et al.*[1] Typically, Ni(NO$_3$)$_2$·6H$_2$O (0.434 g, 1.50 mmol), H$_2$ndc (0.294 g, 1.36 mmol) and dabco (0.336 g, 3.00 mmol) were mixed and dissolved in 30 mL of DMF. After mixing of all the chemicals, a cloudy suspension was obtained, which was transferred to a Teflon-lined autoclave, placed into a preheated oven at 408 K and held at that temperature for 72 hours. The resulting particles were washed several times with fresh DMF.

1.4 Synthesis of deuterated DUT-8(Ni)

The molar ratio of starting materials and the work-up procedure of the resulting crystals is as described in 1.2. However, the amount of starting materials was reduced significantly, due to the expensive linker. The exact procedure is the following:

Typically, Ni(NO$_3$)$_2$·6H$_2$O (65.4 mg, 0.225 mmol, 1.56 eq.) is dissolved in 1.4 mL *N,N*-dimethylformamide (DMF), d6-H$_2$ndc (50 mg, 0.225 mmol, 1.56 eq.) is dissolved 3 mL DMF and dabco (16 mg, 0.14 mmol) is dissolved in 1.1 mL MeOH. The three resulting solutions are combined in a Teflon vessel (50 mL) and heated in an autoclave to 120 °C and annealed for 48 hours.

1.5 Synthesis of mixed metal DUT-8(Ni$_{0.98}$Co$_{0.02}$)

Typically, Co(NO$_3$)$_2$·6H$_2$O (75 mg, 0.028 mmol, 0.03 eq.) is dissolved in 3 mL *N,N*-dimethylformamide (DMF), Ni(NO$_3$)$_2$·6H$_2$O (399.6 mg, 1.372 mmol, 1.53 eq.) is dissolved in 3 mL DMF, 2,6-H$_2$ndc (303.4 mg, 1.4 mmol, 1.56 eq.) is dissolved 15 mL DMF and dabco (100 mg, 0.9 mmol) is dissolved in 9 mL MeOH. The four resulting solutions are combined in a Teflon vessel (50 mL) and heated in an autoclave to 120 °C and annealed for 48 hours. The resulting crystals were washed several times with fresh DMF and subsequently the respective solvent was exchanged.

1.6 Solvent Exchange

All polar solvents were exchanged directly from DMF. To obtain the samples loaded with non-polar solvents (*n*-heptane, cyclohexane and tetrachloromethane), DMF was firstly exchanged to DCM, due to the low miscibility of DMF and the respective solvents. DMF was removed by decantation and the crystals were suspended in the respective fresh solvent. The supernatant solution was removed several times in the first 2 hours and then every 12 hours for another 2 days. For the "repeated switching experiment" the solvent was exchanged 3 times within 30 minutes (Figure 3c,d).

2 Methods

2.1 Powder X-ray diffraction

Powder X-ray diffraction (PXRD) experiments at room temperature were carried out using STOE STADI P diffractometer equipped with a Cu-Kα1 radiation source (λ = 1.5405 Å) and a 2D detector (Mythen, Dectris) in transmission geometry.

2.2 Single crystal X-ray diffraction

The mother liquor containing single crystals of DUT-8(Ni) obtained in the solvothermal synthesis was exchanged to the respective solvent several times in two days and the crystal was sealed in a glass capillary with a small amount of solvent. The datasets for DMF (2010[2]) were collected using a STOE IPDS II image plate diffractometer with Mo–Kα radiation at 293 K and for NMP and toluene at BESSY MX BL14.3 beamline of Helmholtz-Zentrum Berlin für Materialien und Energie with λ = 0.89429 Å at 296 K.[3] The detailed processing procedure is described in section 3.1.

2.3 High-resolution TEM imaging

Samples for TEM investigations were prepared by dropping the "as made" DUT-8(Ni) nanoparticles suspended in DMF onto a carbon coated copper grid and dried at room temperature. TEM studies were performed using a Thermofisher TITAN TEM operated at 300 kV with a Cs-corrector on objective side. High-resolution TEM images were collected at a nominal magnification of 69kx, at electron dose of 11 e/Å^2 per image. The magnification and dose rate were adjusted in order to match the characteristic dose[4] of the material, being measured as 10 e/ Å^2. The images were collected using a self-written Digital Micrograph (GATAN, Pleasanton, USA) script, shifting the TEM stage in a regular grid, thus assuring data collection from a fresh, previously unexposed area. A delay was built into the script after the stage shift before the exposure, in order to minimize the stage-movement induced sample drift.

2.4 ^{2}H solid state nuclear magnetic resonance spectroscopy

^{2}H solid state NMR spectroscopy experiments were carried out using a Bruker 800 MHz Ascend NMR spectrometer at room temperature. The samples were filled in a 2.5 mm zirconium rotor. Spectra were recorded at a resonance frequency of 122.83 MHz for ^{2}H using a triple resonance probe without rotation. The chemical shift was referenced to CDCl$_3$. The used pulse sequence was a WURST QCPMG provided by Rob Schurko.[5] Pulse length was 50 μs with a power level of 1.98 W. The time domain size must be adjusted according to the separation of the spikes. The recycle delay D1 was 500 ms, time to allow pulse ringdown was 17.6 μs and the duration of the echo was 100/300 μs which influenced the separation of the spikes. Number of echoes was 64 per scan. 0 Hz exponential line

broadening and a magnitude function was applied after Fourier transformation to obtain absorptive spikelets.

2.5 Continuous wave electron paramagnetic resonance spectroscopy

The electron paramagnetic resonance (EPR) samples were prepared by filling the DUT-8(Ni$_{0.98}$Co$_{0.02}$) material solvated in DCM, DMF or *n*-heptane together with the corresponding solvent into conventional X-band quartz glass tubes so that the MOF powder was completely covered by the solvent in the EPR tubes. All continuous wave (cw) EPR experiments were performed on a Bruker EMX micro (X-band, 9.4 GHz) spectrometer equipped with an ER 4119 HS cylindrical resonator and an Oxford Instruments He cryostat ESR 900 which enabled low temperature experiments. Spectra were measured always at different microwave powers to ensure no line shape distortions due to saturation effects. The modulation amplitudes were set to 1 mT, which was always significantly smaller than the smallest resolved peak-to-peak line width of the experimental spectra. The experimental EPR spectra were simulated by exact numerical matrix diagonalization of the full spin Hamiltonian, using the corresponding implementation for the simulation of powder spectra of the MATLAB toolbox EasySpin 5.2.25.[6] The determination of the spin Hamiltonian parameters were supported by fitting the simulated EPR spectra to the experimental ones using the nonlinear programming solver *fmincon* provided by the optimization toolbox of MATLAB R2019a. The spectra were baseline corrected in advance by subtracting appropriate polynomials.

3 Single crystal X-ray diffraction analysis

3.1 "As made" single crystals

The main feature of DUT-8(Ni) structure is a non-linearity of the 2,6-ndc^{2-} linker. This leads to a systematic stepwise relocation of pillars in the crystal structure with a constant value of 1.2 Å, dictated by quasi-linear 2,6-naphtalene core. The crystal structure of DUT-8(Ni) was initially determined in 2010 by single crystal X-ray diffraction.[2] The tetragonal space group *P*4/*n* was chosen for the structure solution and refinement, although symmetry of the structure is compatible with high symmetrical space group *P*4/*nmm*. Authors fairly admitted high R-values (R_{int} = 0.2694, R_1 ($I > 2\sigma(I)$) = 0.1546, wR_2 (*all data*) = 0.3428 after SQUEEZE). The local coordination environment of the paddle-wheel is built by four equally oriented 2,6-ndc^{2-} linkers, directed by the 4-fold rotation axis. The crystal structure of the closed pore phase was solved from single crystal X-ray diffraction in triclinic symmetry and further refined from powder X-ray diffraction data. Interestingly, in this case only the conformation with alternating ligand steps could be achieved.[7] Heine and co-workers considered both conformations, called polymorph A (equal to initially published in 2010) and polymorph B (reported in 2015) and suggested the most appropriate closing mechanism involving the structures of conformer B.[8] The results were also supported by an experimental structure, derived from single crystal data. The structure of conformation B was refined in the monoclinic space group *C*2/*m* with acceptable final reliability parameters (R_{int} = 0.0581, R_1 ($I > 2\sigma(I)$) = 0.0826, wR_2 (*all data*) = 0.2625), but considering pseudo-merohedral twinning in the sample (rotation matrix 1 0 0.5   0 −1 0   0 0 −1). All these findings confirm the complexity of the crystal structure of DUT-8(Ni) and stimulated us to deeper investigate the domain structure in the system. As a first step we reinvestigated the data reported in 2010.[2] Careful analysis of (hk0), (hk1), (hk2) and (hk3) lattice planes indicate the co-existence of multiple domains in the single crystal (Fig. S1).
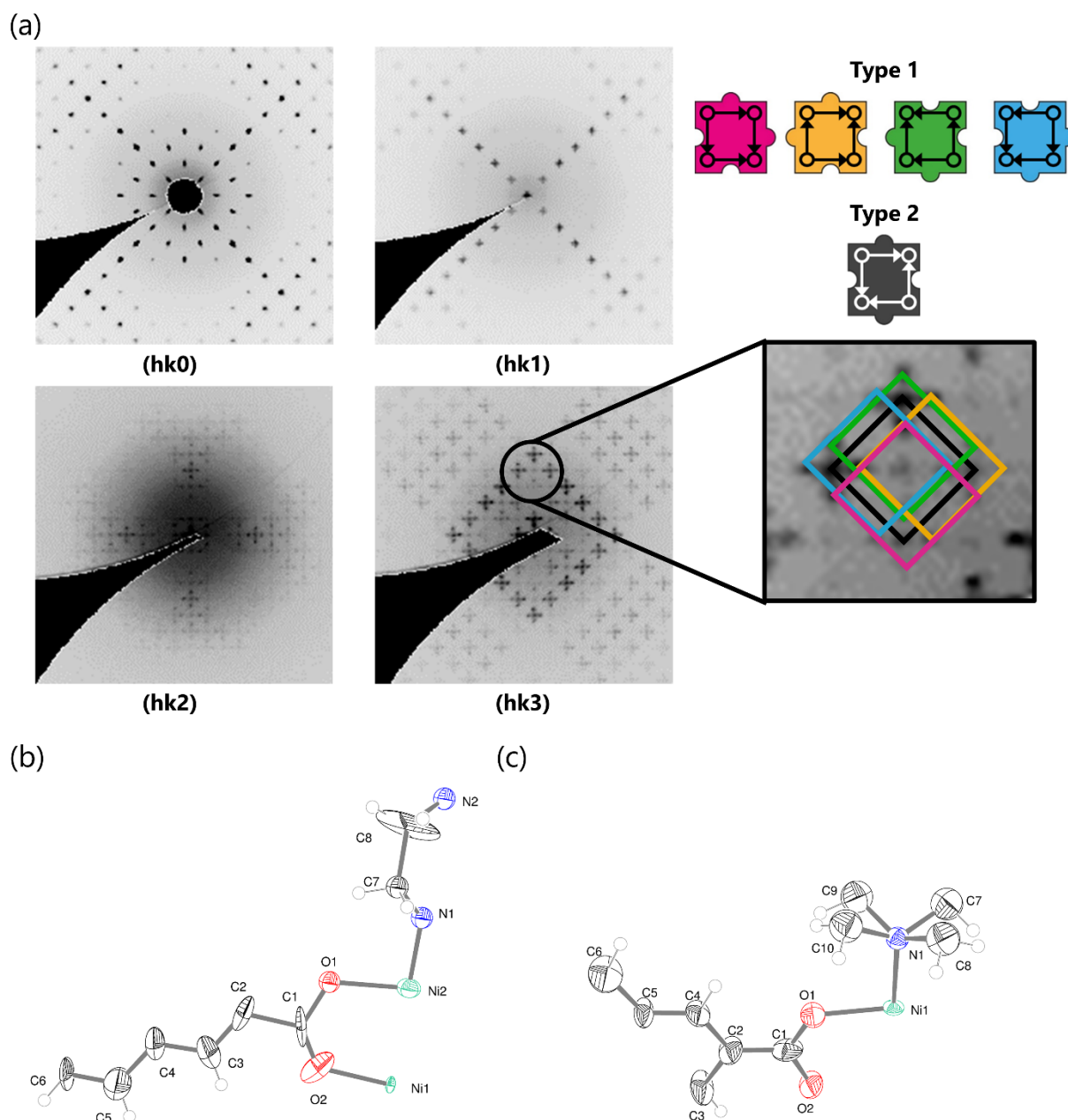
Figure S1. (a) Representation of (hk0), (hk1), (hk2) and (hk3) reciprocal lattice planes, indicating the presence of both monoclinic (type 1, C_{2h}) and tetragonal (type 2, D_{2d}) domains in the structure; ORTEP diagram of asymmetric unit for tetragonal (b) and monoclinic (c) structures. Ellipsoids are shown at a 50% probability level.

Depending on the lattice selection, the dataset was processed in tetragonal (*P*4/*nmm*) and monoclinic (*C*2/*m*) symmetry. In both cases, the crystal structure was solved by direct methods and refined by least-squares on F^2 using SHELX-2018.[9] The corresponding structural models correspond to conformers A and B, discussed elsewhere in detail.[8] Similar unit cell volumes for both structural models allow their co-existence within the same single crystal. The convergence parameters of the refinement in both cases are not acceptable in terms of reliability factors and residual electron density, which cannot be attributed to chemically reasonable atom positions of the structures (Table S2). Since both monoclinic and tetragonal domains are simultaneously present in the reciprocal space leading to overlapping in numerous reciprocal lattice planes, we decided not to continue further analysis of the data (Section 4). CCDC-1989709 and CCDC-1989708 contain the supplementary crystallographic data for DUT-8(Ni) polymorph A and DUT-8(Ni) polymorph B, respectively. ORTEP diagrams show the asymmetric units of both structures are shown in Figure S1b-c.

Table S2. Experimental data on DUT-8(Ni) single crystal, solved and refined from the same dataset in tetragonal and monoclinic symmetries.

	Polymorph A Refinement	Polymorph B Refinement
Empirical formula	$C_{30} H_{24} N_2 Ni_2 O_8$	$C_{30} H_{24} N_2 Ni_2 O_8$
Formula weight	657.93	657.93
λ, Å	0.71073	0.71073
Crystal system, space group	tetragonal, *P4/nmm*	monoclinic, *C2/m*
Unit cell dimensions, Å	a = 18.431(3) c = 9.3882(19)	a = 18.563(4) b = 18.416(4) c = 9.3815(19) β = 96.41(3)
Volume, Å^3	3189.2(11)	3187.0(11)
Z	2	2
ρ, g/cm^3	0.685	0.686
μ, mm^{-1}	0.615	0.615
$F(000)$	676	676
θ range, deg	2.17 – 30.63	2.18 – 30.98
Limiting indices	$-26 \leq h \leq 26$ $-26 \leq k \leq 26$ $-13 \leq l \leq 11$	$-26 \leq h \leq 26$ $-26 \leq k \leq 26$ $-11 \leq l \leq 13$
Reflections collected / unique	50271 / 2695	25941 / 3538
R(*int*)	0.2869	0.2856
Data / parameters	2695 / 73	5020 / 120
GooF on F^2 [$I>2\sigma(I)$]	1.842	1.267
Final R indices [$I>2\sigma(I)$], R1, wR2	0.2738, 0.5321	0.2106, 0.4411
R indices (all data), R1, wR2	0.3020, 0.5584	0.2832, 0.4967
Largest diff. peak / hole, eÅ^{-3}	11.099 / -1.851	9.928 / -2.751

3.2 Solvent exchanged single crystals

Single crystals of DUT-8(Ni) were analysed, in which guest molecules were exchanged from DMF to N-methyl-2-pyrrolidone (NMP) or toluene. According to PXRD patterns, these samples contain predominantly C_{2h} loops (ϕ = 0.1, η = 0.1), which can be treated in the refinement as pseudo-merohedral twins with partially overlapped reciprocal lattices. The datasets were collected at BL14.3 beamline of the BESSY-II synchrotron.[10] For each single crystal, 180 images were collected in a φ-scan mode with an oscillation angle of $\Delta\varphi$ = 1°. A Rayonix MX-225 detector at 55 mm distance was used to collect the 2D images with 1.2 s exposition. The collected images were processed in

automatic mode using XDSAPP 2.0 software.[11] Alternatively, images were converted in .sfrm format and four partially overlapped monoclinic C-centred lattices were found using CELL_NOW program.[12] The images of (hk0), (hk1), (hk2) reciprocal planes confirm the presence of four different domains in both single crystals (Fig. S2). The intensities were extracted using SAINT software[13] and corrected for absorption, Lorentz and polarization effects using TWINABS program[14]. Two separate files, one containing structural factors from single domain for structure solution (HKLF4 format) and second with reflections of all four domains for structure refinement (HKLF5 format) were generated. The structures were solved using direct methods and refined by least-squares on F^2 using SHELX-2018/3 software.[9] The dabco molecules show dynamic disorder with 8 separate positions for three carbon atoms and therefore refined with occupancies 3/8 for each general position. The volume fractions of each domain in the structure were refined as free variables resulting in a ratio 0.325(4) / 0.325(4) / 0.209(3) / 0.141(3) for NMP@DUT-8(Ni) crystal and 0.297(4) / 0.294(4) / 0.200(3) / 0.209 (3) for toluene@DUT-8(Ni). CCDC- 1989557-1989560 contain the supplementary crystallographic data for NMP@DUT-8(Ni) and toluene@DUT-8(Ni), respectively. The ORTEP diagrams of asymmetric unit for all structures are shown in Figure S2c-f.
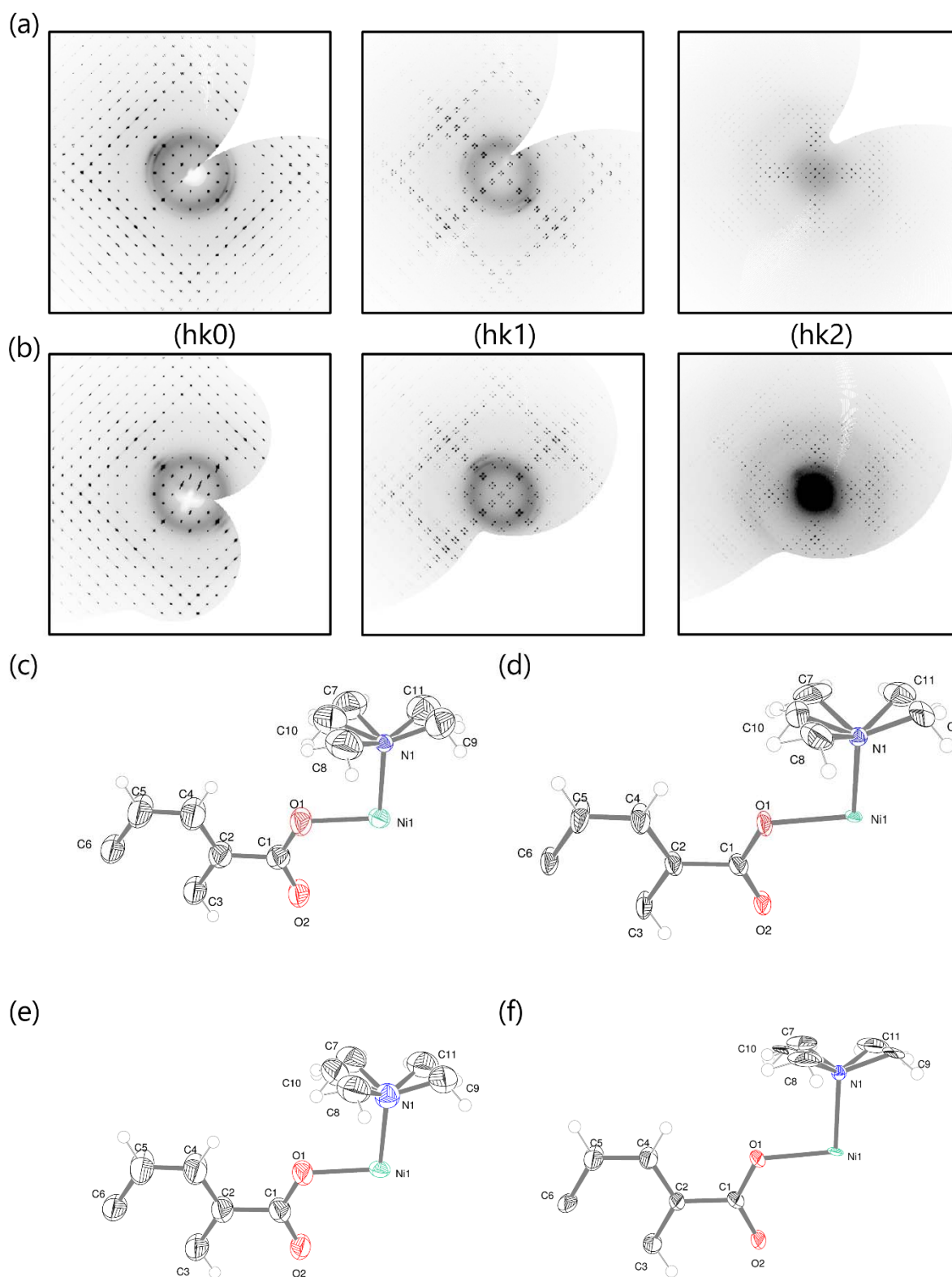
Figure S2. Representation of (hk0), (hk1) and (hk2) reciprocal planes for NMP@DUT-8(Ni) (a) and toluene@DUT-8(Ni) (b); ORTEP diagrams of asymmetric unit of NMP@DUT-8(Ni) single domain (c), NMP@DUT-8(Ni) twin refinement (d), toluene@DUT-8(Ni) single domain (e), toluene@DUT-8(Ni) twin refinement (f). Ellipsoids are shown at a 50% probability level.

Table S2. Experimental data on NMP@DUT-8(Ni) and toluene@DUT-8(Ni) single crystals, treated as a single domain and refined as a four-component twin (Empirical formula: $C_{30}H_{24}N_2Ni_2O_8$, formula weight = 657.93 g/mol).

	NMP@DUT-8(Ni) single domain	NMP@DUT-8(Ni) twin refinement	toluene@DUT-8(Ni) single domain	toluene@DUT-8(Ni) twin refinement
λ, Å	0.89429	0.89429	0.89429	0.89429
Crystal system, space group	monoclinic, $C2/m$	monoclinic, $C2/m$	monoclinic, $C2/m$	monoclinic, $C2/m$
Unit cell dimensions, Å	a = 18.700(4) b = 18.340(4) c = 9.3900(19) β = 96.82(3)	a = 18.682(4) b = 18.322(4) c = 9.3843(19) β = 96.82(3)	a = 18.540(4) b = 18.410(4) c = 9.3200(19) β = 98.66(3)	a = 18.554(4) b = 18.419(4) c = 9.3244(19) β = 98.62(3)
Volume, Å^3	3197.6(11)	3189.4(11)	3144.8(11)	3150.5(11)
Z	2	2	2	2
ρ, g/cm^3	0.685	0.685	0.695	0.694
μ, mm^{-1}	1.138	1.141	1.157	1.155
$F(000)$	676	676	676	676
θ range, deg	1.96 – 33.94	1.96 – 33.94	1.97 – 33.96	1.97 – 33.98
Limiting indices	$-23 \leq h \leq 23$ $-22 \leq k \leq 22$ $-11 \leq l \leq 11$	$-26 \leq h \leq 26$ $0 \leq k \leq 22$ $0 \leq l \leq 11$	$-19 \leq h \leq 23$ $-22 \leq k \leq 22$ $-11 \leq l \leq 11$	$-23 \leq h \leq 22$ $0 \leq k \leq 22$ $0 \leq l \leq 11$
Reflections collected / unique	11124 / 3356	- / 10890	10949 / 3244	- / 10329
R(*int*)	0.0528	-	0.0621	-
Data / parameters	3356 / 121	10890 / 124	3244 / 121	10329 / 124
GooF on F^2 [$I>2\sigma(I)$]	1.528	1.087	1.794	1.279
Final *R* indices [$I>2\sigma(I)$], *R1, wR2*	0.1660, 0.3841	0.1002, 0.3115	0.1904, 0.4368	0.1201, 0.3545
R indices (all data), *R1, wR2*	0.1753, 0.3946	0.1319, 0.3364	0.1952, 0.4468	0.1314, 0.3777
Largest diff. peak / hole, *e*Å^{-3}	7.224/ -2.402	1.361 / -1.777	11.343 / -3.340	0.991 / -2.852

4   Generation of the disorder models

The strikingly rich structural variety in DUT-8 arises from the step function implicit to the 2,6-ndc linker embedded in the DUT-8(Ni) framework structure (Figure 1a). DUT-8(Ni) belongs to the pillared layer structures, which in case of linear linkers typically form regular planar tetragonal (4,4) nets of composition $[M(O_2C-R-CO_2)_{4/2}]_\infty$ which are pillared by linear N-donor ligands (dabco). However, the step function in DUT-8(Ni) imposes deviations from planarity and considering the paddle-wheel nodes the linker can form a step-up or step-down function. A straightforward representation of the step-function is an arrow pointing upwards (Figure S3).

In a periodic network structure, the registry requirement for closed loops places a non-trivial constraint on the vectors in that loop and it can be shown that only six local configurations are allowed. They can be classified into 4 equivalent configurations with local symmetry 2/m (C_{2h}) which are related to each other by rotations around the 4-fold axis, in the following denoted as "Type 1" or "C_{2h}", while 2 remaining configurations have $\bar{4}m2$ (D_{2d}) symmetry ("Type 2").
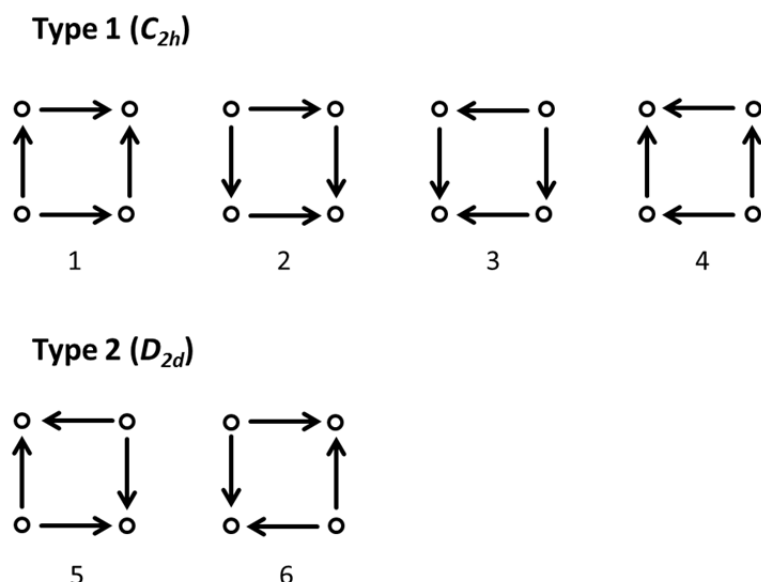

Figure S3. Representation of type 1 (C_{2h}) and type 2 (D_{2d}) loops satisfying the registry requirement for closed loops.

Each loop may be also represented by a tile with characteristic tongue-groove orientation by rotating the arrows by 90° counter-clockwise (Figure S4)
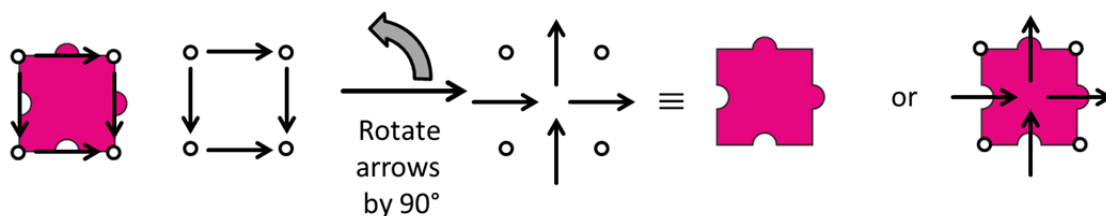

Figure S4. Representation of loops by coloured tiles with tongue and groove.

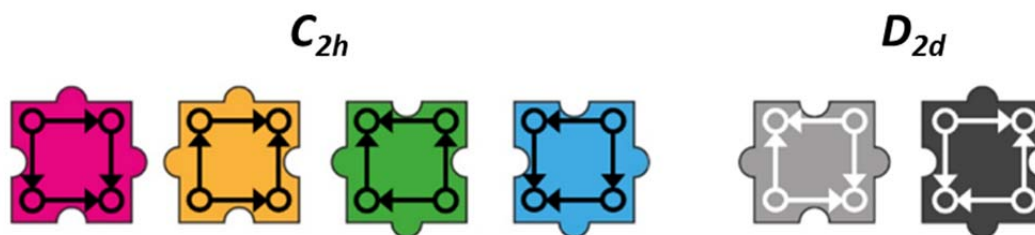The equivalence of arrow-loops and coloured tiles is displayed in figure S5a.

Figure S5a. Transformation of the 6 loops into colour-coded tiles.

It is also important to note the implications of the periodic tiling on the local paddle-wheel (PW) configuration (Figure S5b). Each of the four ndc linkers connected to one PW may point upwards (+) or downwards (-) denoting the relative neighbouring orientation which allows for four different local PW configurations (**a**: $+ + + +$, **b**: $+ + - -$, **c**: $+ - + -$, **d**: $+ - - -$).
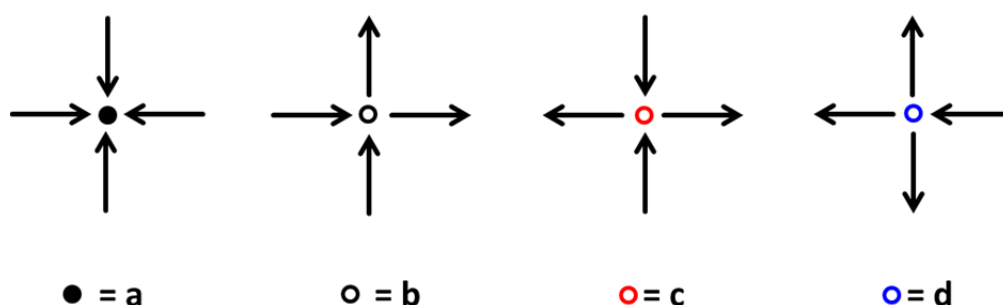

Figure S5b. Local paddle-wheel variants.

Each individual C_{2h} loop can tile space by itself to form a periodic arrangement with 2D crystal class m. Each paddle-wheel cluster in this structure contains two 2,6-ndc pointing "up" and two pointing downwards in *cis*-orientation (or "$+ + - -$", polymorph **B**, monoclinic, containing PWs **b**, local symmetry *2/m*, Figure S6).[8] D_{2d} loops cannot by themselves tile space, instead the unique extended lattice containing D_{2d} configurations belongs to the 2D crystal class *4mm*. In this structure all 2,6-ndc linkers surrounding one paddle-wheel have the same orientation ("$+ + + +$", polymorph **A,** PW **a**), tetragonal, local symmetry *4mm*). The "up and down" orientation alternates between adjacent clusters.
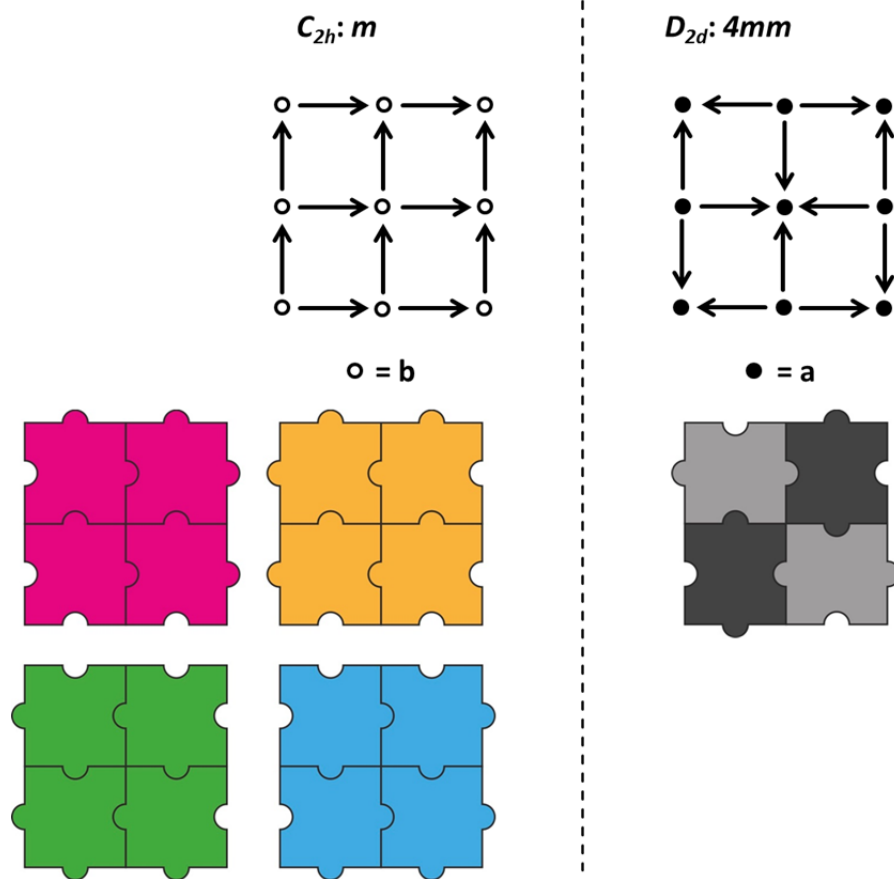
Figure S6. Transformation of the 6 loops into color-coded tiles.

It is important to note that **A** and **B** characterize here the **periodic structure** obtained by arranging the tiles into a periodic pattern while **a** and **b** denote here the **local arrangement of linkers for a single paddle-wheel** (PW). It will be shown below in which cases local arrangements **c** and **d** are formed in disordered configurations of tiles.

The six configurations are equivalent to the six "2-in-2-out" states of the square-ice spin model[15] with a finite configurational entropy $S_{config} = R \cdot \ln\left(\frac{4}{3}\right)^{\frac{3}{2}} \cong 0.43R$, hence favoring disorder in DUT-8 at 300 K by ca. 1 kJ/mole of Ni-dabco chains.

To rationalize an adequate disorder model, in a first approximation we only consider C_{2h} loops in a supercell. We assign the probability ϕ that denotes the likelihood of neighbouring rows/columns sharing opposite 2,6-ndc orientation. A probability $\phi = 0$ corresponds to the ordered m configuration (C_{2h}, m). A probability $\phi = 1$ gives another ordered configuration with tetragonal symmetry (2D crystal class $4mm$). Note, that this is another tetragonal variant without D_{2d} loops but containing PW **a** and **c** ("$+ - + -$") with local symmetry $\bar{4}$. A probability $\phi = 0.5$ gives a statistical distribution of row/column 2,6-ndc configurations.
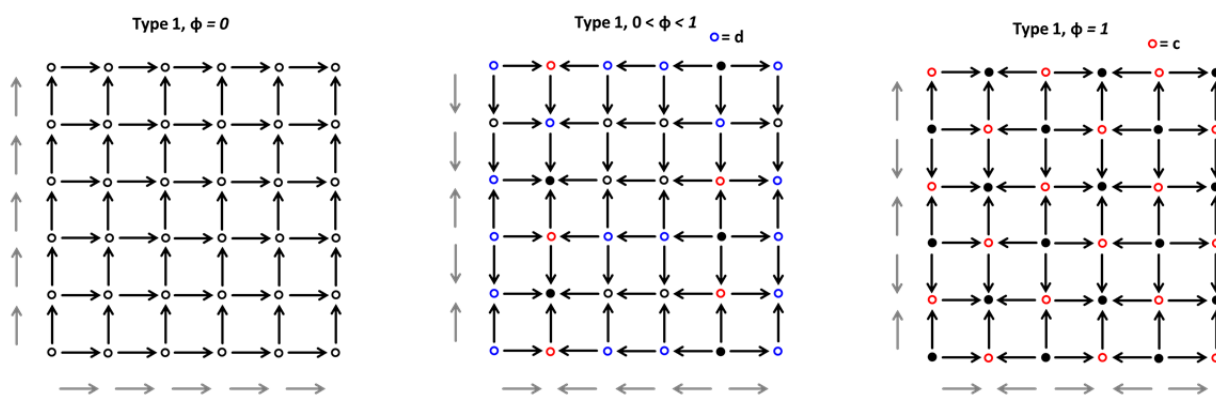

Figure S7. Illustration of the probability ϕ for a 5x5 superstructure in 3 representative disorder configurations only containing type 1 (C_{2h}) loops.

Interestingly, these intermediate ϕ values ($0 < \phi < 1$) generate the fourth PW variant **d** with three 2,6-ndc linkers oriented in one direction ("$+ + + -$"). For a superstructure consisting of N PWs the number of possible combinations is W^N and $W = \left(\frac{4}{3}\right)^{\frac{3}{2}}$.[15] This is the basis of disorder adaptivity providing a countably infinite number of disorder configurations as a response to a molecular stimulus. As orientations of the rows/columns may be indexed as a binary code, (01110) in principle the complex structural disorder in DUT-8 resembles a binary storage system. Lines at which columns with opposite orientation hit each other can be considered as C_{2h} domain boundaries.

As will be shown below, for the modelling of the experimentally observed powder patterns it is necessary to construct models containing interspersed D_{2d} loops. They are essentially generated by flipping individual arrows in a C_{2h}-loop-only configuration. The relative fraction of D_{2d} loops is η.

Figure S8 shows a representative real world structure as a paradigmatic 16x16 supercell, originally composed of C_{2h}-loops (original row/columns orientations indicated with grey arrow). Flipping individual arrows in this example creates tetragonal microdomains composed of D_{2d}-loops and domain walls at the intersection. The center of the tetragonal microdomains is located at the intersection of the type 1 domain boundaries.
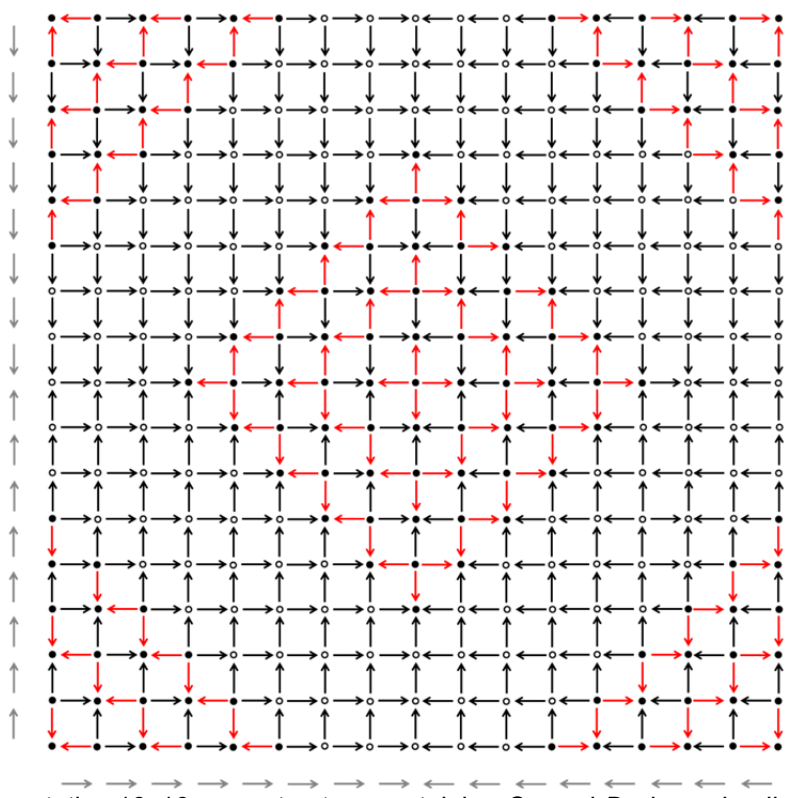
Figure S8. Representative 16x16 superstructure containing C_{2h} and D_{2d} loops leading to the formation of microdomains.

5   Calculation of X-ray diffraction patterns

A custom Monte Carlo code was implemented to generate DUT-8 configurations of arbitrary size with specific (ϕ,η) characteristics. Simulations were initialized in the type 2 (D_{2d}) phase. Monte Carlo steps involved the 'long loop' algorithm, which ensured that square ice rules were strictly obeyed at all times.[16] The Monte Carlo criterion was based on the difference between calculated and target (ϕ,η) values. The simulation was terminated when the target (ϕ,η) value of interest was reached. Simulation boxes of 40 x 40 supercells were used. At this size, the increasingly ordered configurations were difficult to access, which is why we had difficulty obtaining configurations corresponding to the edges of the phase triangle (Figure 3b). For each generated DUT-8 configuration a model was simulated using a Monte Carlo approach. This model contains a single atom at the vertex of each pore: this corresponds to the midpoint of the Ni-carboxylate paddle-wheel. There is also an atom at the center of each 2,6-ndc unit. We used atom types Nd and Y, respectively, for these two positions since the ratio of atomic masses reflects approximately the ratio of the scattering density of the paddle-wheel and 2,6-ndc units. The unit cell parameters were calculated by taking into account the number of up/down vertical shifts along each direction of the supercell. No attempt was made to convert cells and coordinates into conventional space group form. For each configuration corresponding X-ray diffraction pattern were calculated (λ = 1.541Å) using the program CrystalDiffract (Figure 3a and S9). A peak width of 0.15° was used. We show here the form of the diffraction pattern for 9 °$\leq 2\theta \leq$ 18° for our various Monte Carlo configurations. These patterns are arranged in order of decreasing η (top is η = 1, bottom is η = 0) and by increasing ϕ for common η. So the very lowest diffraction pattern is for type 1(m) (C_{2h}) and the very highest pattern is for type 2 (D_{2d}).
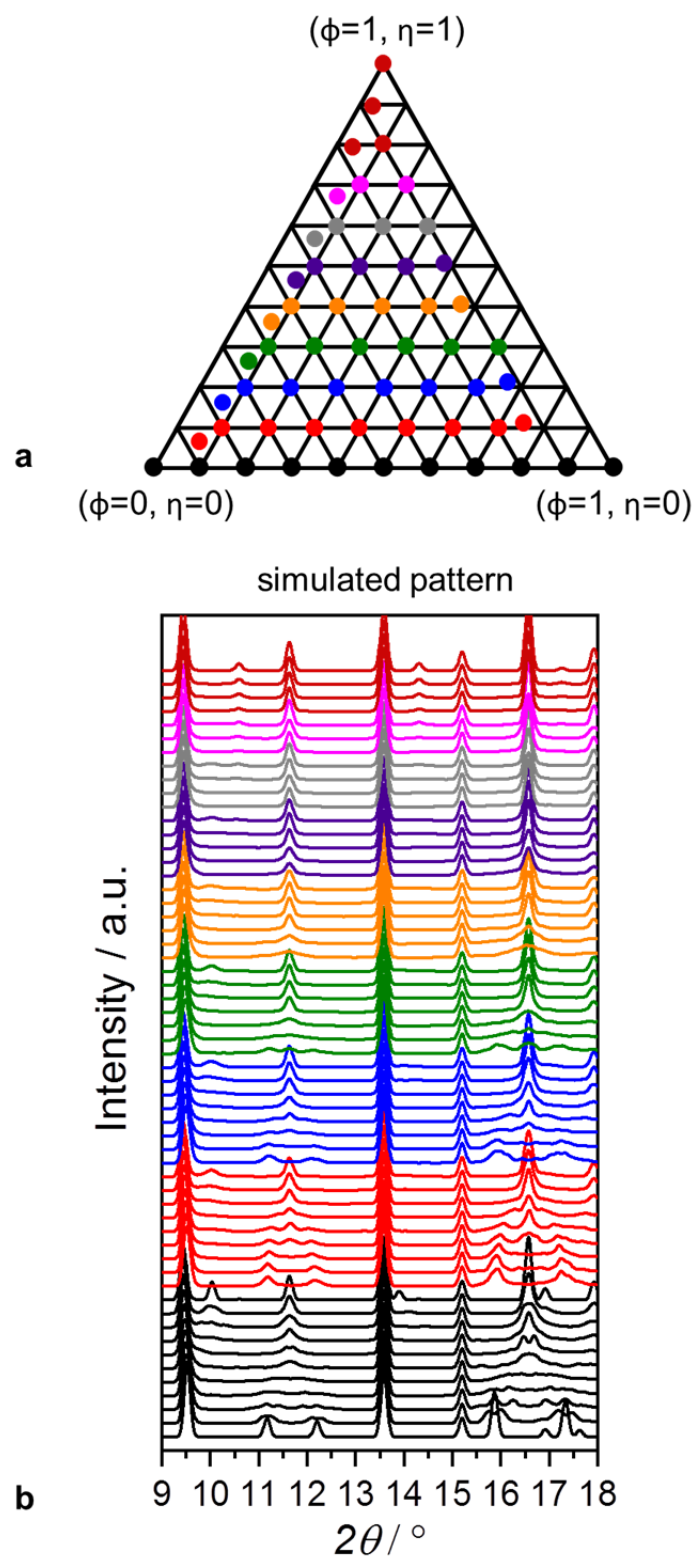
16

Figure S9. Simulated PXRD patterns for disorder models with $0 \leq \phi \leq 1$ and $0 \leq \eta \leq 1$.

6 Experimental X-ray powder patterns

The experimental data sets provided were prepared for comparison by removal of a linear background and rescaling to uniform total integrated intensity across the $9\,°\leq 2\theta \leq 18°$ region. We explored using a number of quantitative approaches by which to automatically match experiment with calculated patterns, but because of subtle variation in peak positions and the inability to match quantitatively the (Bragg) peak intensities, it was not possible to arrive at a universally acceptable solution. Instead we matched patterns by visual comparison.

It is perhaps worth emphasising that the entire ensemble of fits shown in Fig. 3 involves a total of 24 parameters: the peak width, the three structural parameters shown above for the basic connectivity, and the pair of (ϕ,η) parameters for each phase. The values of these disorder parameters are given in the following table S3.

Table S3. Characteristic disorder configurations stimulated by solvent exchange.

Solvent	(ϕ,η)
Acetone	(0.2; 0.1)
Chloroform	(0.4; 0.0)
Cyclohexane	(0.3; 0.3)
Dichloromethane	(0.9; 0.7)
Dimethylformamide, methanol (as synthesized)	(0.4; 0.3)
Dimethylformamide	(0.3; 0.1)
Ethanol	(0.2; 0.2)
n-Heptane	(0.3; 0.2)
N-Methyl-2-pyrrolidone	(0.1; 0.1)
Tetrachloromethane	(0.4; 0.0)
Toluene	(0.1; 0.1)

For some cases these assignments can be made uniquely with confidence; for others there is more than one pair of ϕ,η-values that could account for the observed diffraction pattern. This is probably most severe for the cases of $CHCl_3$, CCl_4, and DMF.

Samples containing low boiling solvents (CH_2Cl_2, $CHCl_3$, CCl_4) in Fig. 3a were prepared in capillaries (measurement time 16-24h). For the dynamic exchange demonstrated in Fig. 3d, in order to measure a pattern directly after the exchange, the samples were prepared between aluminium coated polyester foils and measured within 30 minutes.

In Figure S10a these distinct disorder patterns characteristic for each solvent are located in the ϕ,η triangle and pictorial representations for each disorder pattern are displayed for representative solvents.
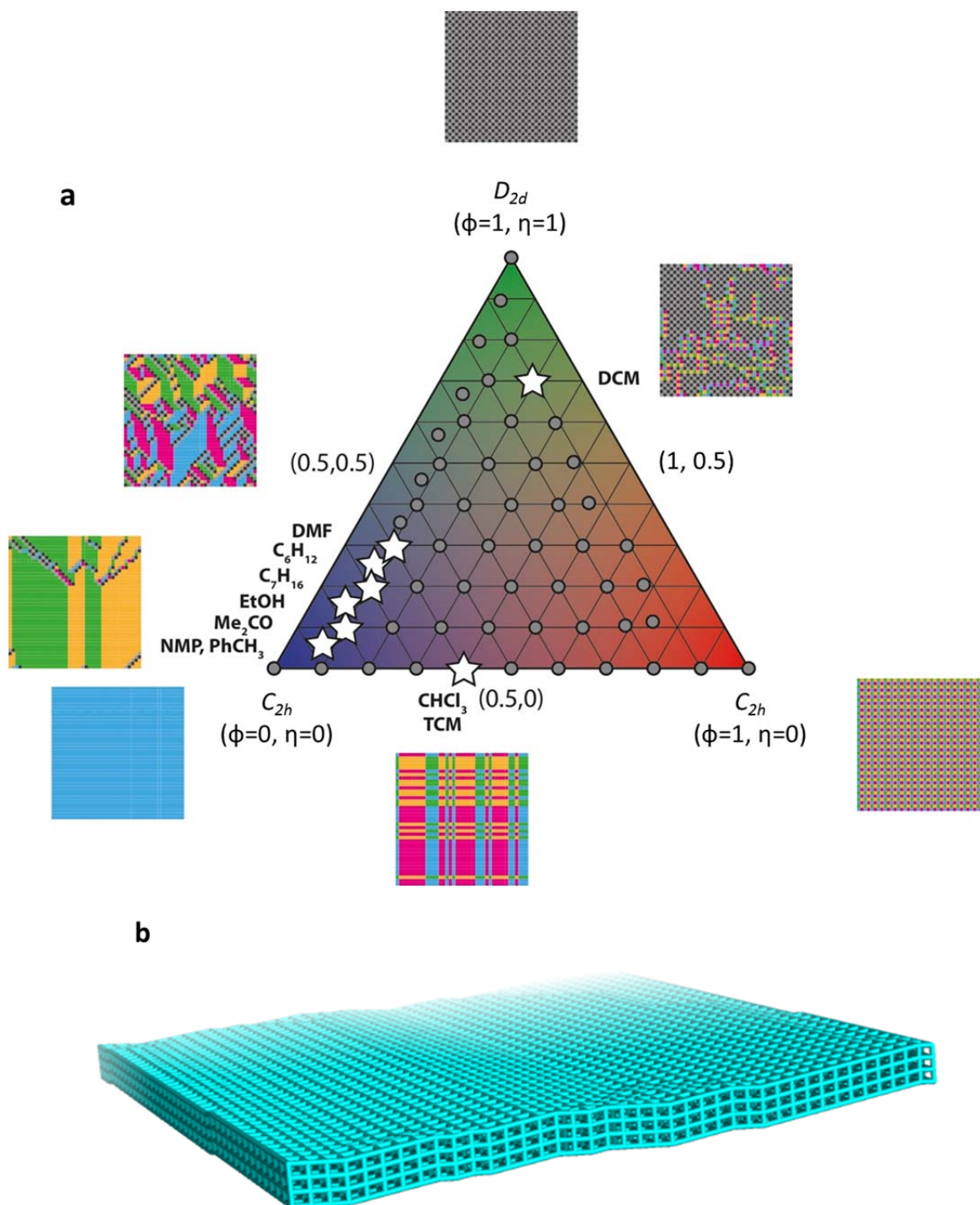

Figure S10. a Localization of disorder configurations in $\phi-\eta$ space. Each coloured tiling illustrates a guest-specific characteristic disordered state. **b** Lateral view of a representative disorder configuration.

Each disorder configuration leads to a characteristic arrangement of PWs (Figure S10b) resulting in a specific undulated surface texture.
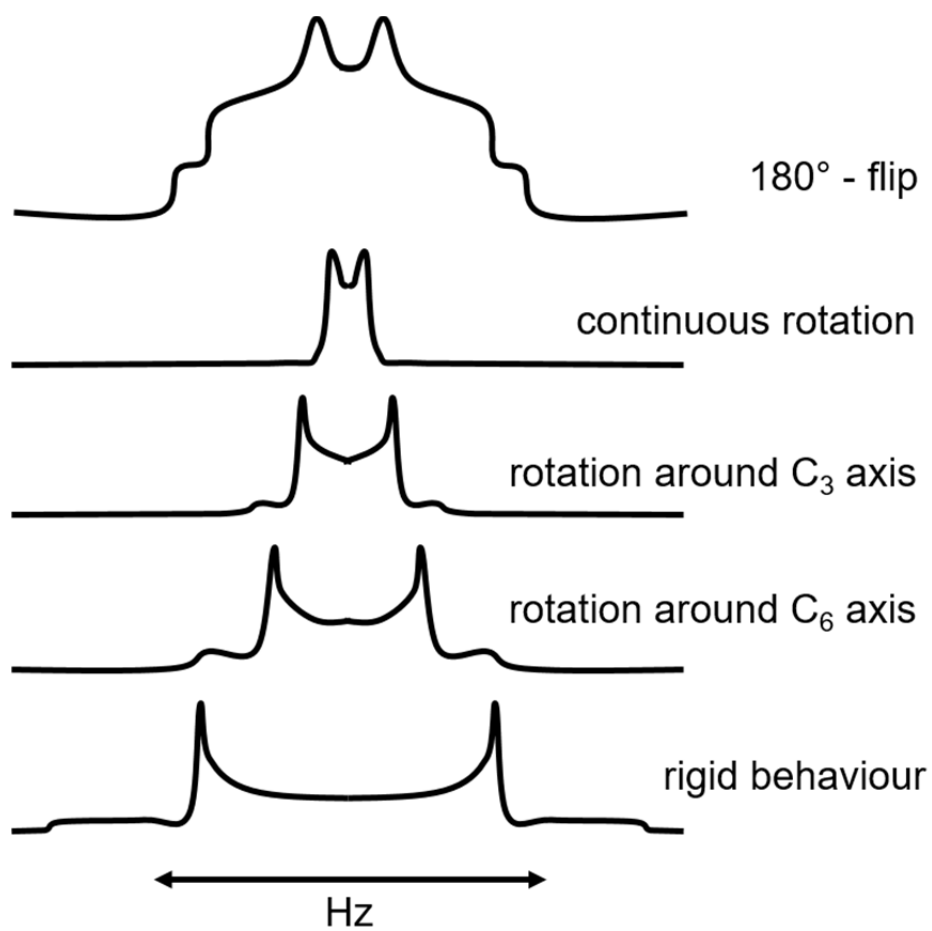
7 Simulated ^{2}H NMR spectra

Figure S11. Simulated NMR spectra for various scenarios differing in linker dynamics.

8 Desolvation experiments and pore closing mechanism analysed by in situ PXRD
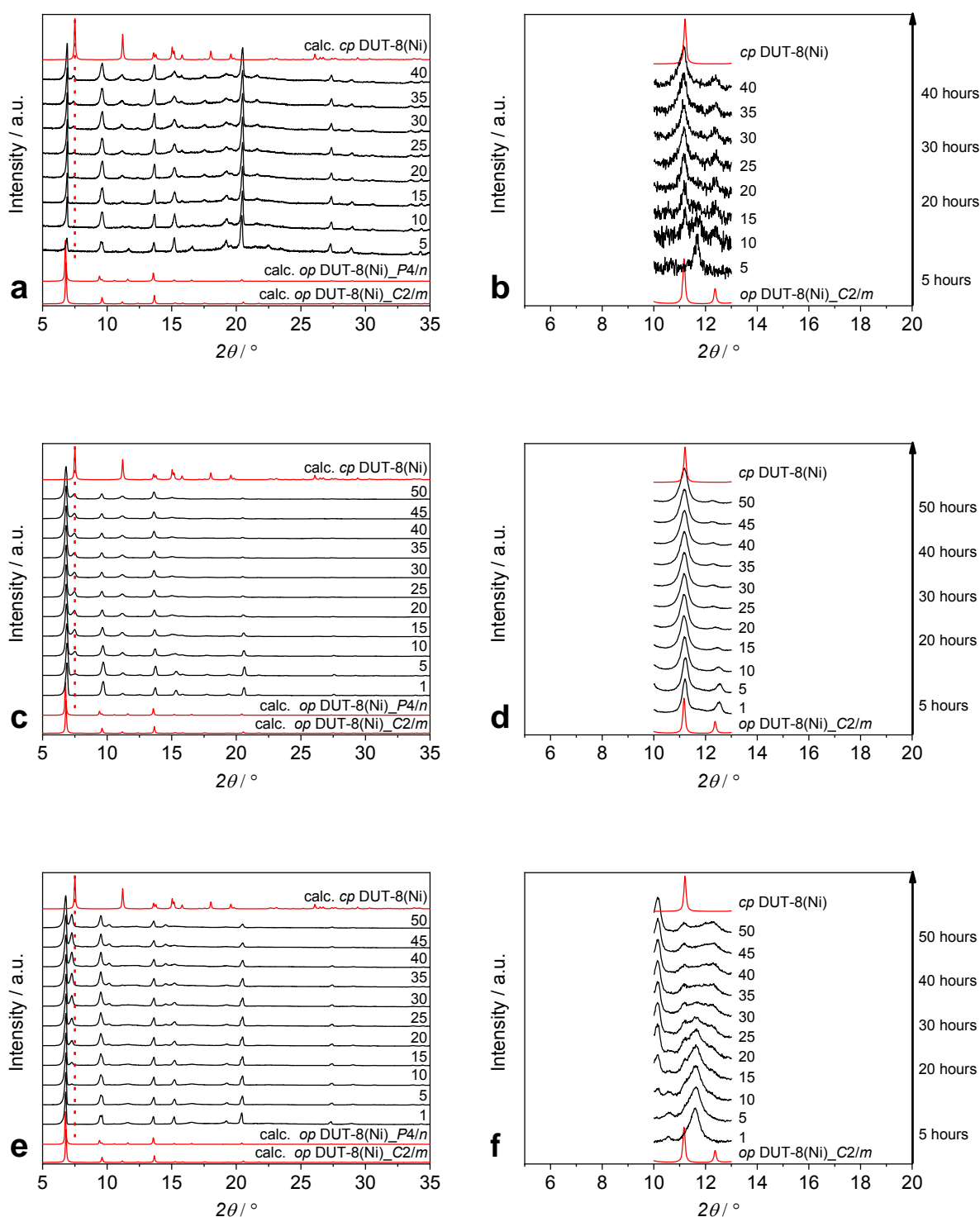

Figure S12. In situ PXRD desolvation experiments of DUT-8(Ni) loaded with various solvents. **a** DCM, **c** *n*-heptane and **e** DMF. For a better representation in **b**, **d** and **f** sections in the range of 10° - 13° are shown. The calculated diffractograms of the *op*- and *cp*-phase of DUT-8(Ni) are shown in red. The numbers indicate the measurement run, and each measurement lasts 75 minutes.

DCM with a high adsorption enthalpy ($|\Delta_{\mathrm{ads}}H| = 35 - 50 \; kJ \; mol^{-1}$)[17] and dipole moment (1.8 D)[18] is the only solvent that favours the formation of D_{2d} loops ("polymorph A", tetragonal, (ϕ = 0.9, η = 0.7)) which according to Petkov *et al.* is energetically slightly favoured by 16 kJ/mol per unit cell as

compared to the C_{2h} loops in polymorph B.[8] However these simulations do not take into account solvent filling.[8] In the same study, the authors showed that the $op\rightarrow cp$ transformation of DUT-8(Ni) for pure D_{2d} loops of the A polymorph is thermodynamically unfavourable unless linker rotation would convert D_{2d} into C_{2h} loops before pore closing.

However, experimental data show that the network filled with DCM containing a high fraction of D_{2d} loops can be desolvated transforming into a *cp*-phase. Therefore, we performed *in situ* PXRD measurements to analyse the structural changes during evaporation of the solvent and the associated transformation of the network. The measurements were performed with samples loaded with DCM, DMF and *n*-heptane. For this purpose, the samples were loaded with the appropriate solvent and transferred into the desolvation chamber. Subsequently, 40 (DCM) and 50 (DMF, *n*-heptane) measurements were carried out one after the other without heating. One measurement took 75 minutes and Figure S12 shows a selection of the runs for the three different samples.

To avoid rapid evaporation, the DUT-8(Ni)_DCM sample was additionally covered with a Kapton® (polyimide) film. As already shown in the previous measurements, DUT-8(Ni) loaded with DCM shows the signature of the tetragonal structure (D_{2d}-loops), which is still clearly discerned after the fifth measurement (6 h 15 min) (Figure S12a,b). After the 10th measurement (12 h 30 min) three reflections in the range between 10° - 13° are detected indicating structural transformation. The middle one can still be assigned to the tetragonal phase and the two outer ones to the monoclinic C_{2h}-loops. After 20 measurements (25 h) only the monoclinic phase is visible and a small peak (7.52°), which can be assigned to the *cp*-phase of DUT-8(Ni) is visible. During the following measurements the network closes further, as evident from the intensity increase of the peak at 7.52°. A complete closing of the structure is not achieved under these mild desolvation conditions but the mechanism is evident: D_{2d} loops of polymorph A transform into C_{2h} loops of polymorph B while being filled with DCM prior to desolvation and transformation into the triclinic *cp*-phase.

The sample loaded with *n*-heptane right from the beginning shows two peaks in the range of 10° - 13°, which can be assigned to the monoclinic phase. After five measurements (6 h 15 min) the peak of the *cp*-phase is visible, which shows a significant increase in intensity during the experiment. An exact comparison of the monoclinic peaks of the calculated structure and DUT-8(Ni)_Heptane (Figure S12c,d) shows that the distance between the two peaks differs slightly. The position of the peak at 11.2° (111) remains unchanged during the activation process, but a clear shift of the peak at 12.5° (11-1) can be seen in the course of the experiment until it almost completely vanishes at the end of the experiment. This peak is also not present in the calculated *op*-phase of DUT-8(Ni), which suggests that a large part of the sample has already passed into the *cp*-phase by the simple evaporation of the solvent.

The sample, which is loaded with DMF, shows a strongly broadened peak (11.6°), with an evolving small shoulder after about 15 measurements (16 h 45 min) (Figure S12e). In the further course, clear domains are formed. As with DCM, the D_{2d} dominated regions of the sample transform into the monoclinic structure dominated by C_{2h} domains during further evaporation of the solvent.

The in situ PXRD measurements demonstrate that a transformation of D_{2d} loops in "polymorph A" into C_{2h} loops in "polymorph B" takes place during desolvation by passing through the ϕ,η landscape. This happens before the solvent is completely removed from the pore channels. In agreement with the considerations of Petkov *et al.* transformation of polymorph A into B is energetically favoured before the pore closing from the *op*- to the *cp*-phase is observed.

9 EPR experiments on solvated Co^{2+} doped DUT-8(Ni$_{0.98}$Co$_{0.02}$) samples

Table S4. Experimentally derived effective g-tensor and Co^{59} hyperfine-interaction (hfi) principal values of the spin Hamiltonians assigned to EPR active species A$_{DCM}$ and A$_{DMF}$ in DUT-8(Ni$_{0.98}$Co$_{0.02}$)_DCM and DUT-8(Ni$_{0.98}$Co$_{0.02}$)_DMF samples.

Species	g_x	g_y	g_z	A_x / MHz	A_y / MHz	A_z / MHz
A$_{DCM}$	2.653(6)	2.600(6)	1.772(3)	528(10)	506(10)	390(5)
A$_{DMF}$	2.740(10)	2.589(10)	1.753(3)	550(20)	462(20)	423(10)

Table S5. Effective g-tensor and Co^{59} hyperfine-interaction (hfi) principal values of the spin Hamiltonians assigned to EPR active species A1$_{heptane}$ and A2$_{heptane}$ in DUT-8(Ni$_{0.98}$Co$_{0.02}$)_heptane as suggested by a least square fit of the simulated to the experimental EPR spectrum. The simulation derived relative amount of A1$_{heptane}$: A2$_{heptane}$ is 2:1. Large errors of the parameters correlate with large anisotropic inhomogeneous broadening of the respective values.

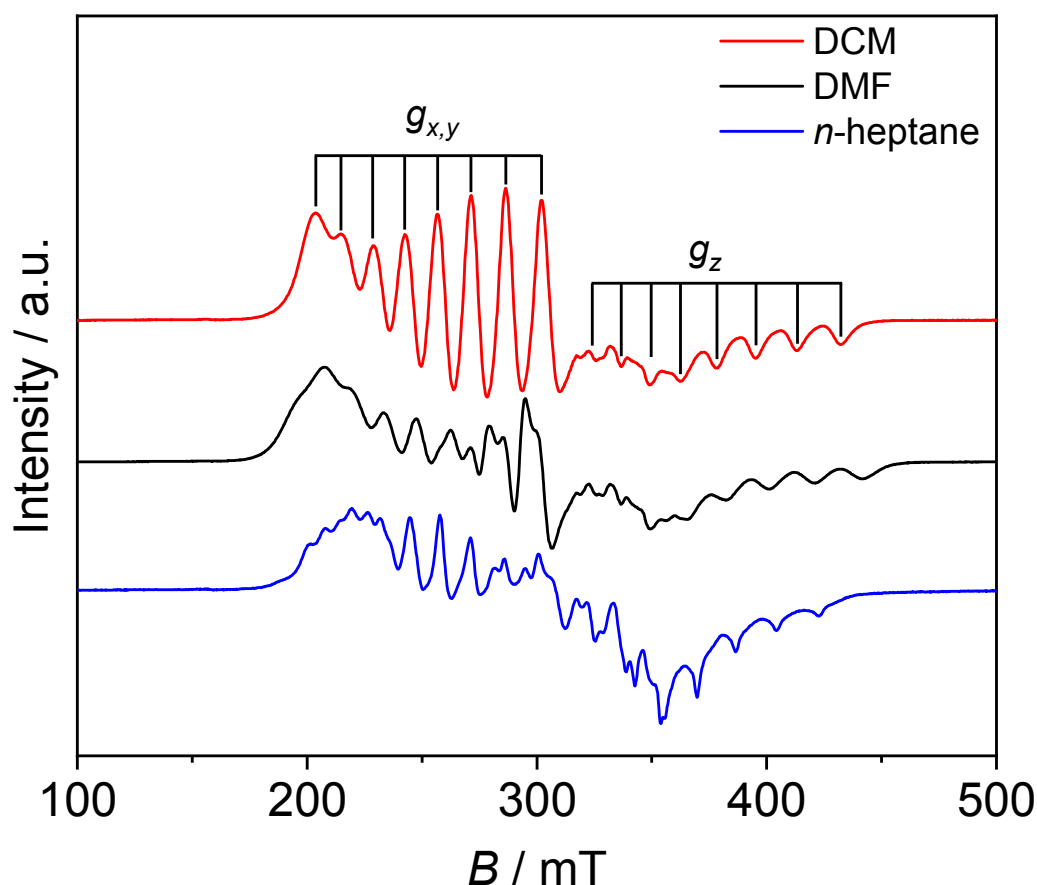| Species	g_x	g_y	g_z	A_x / MHz	A_y / MHz	A_z / MHz
A1$_{heptane}$	2.607(10)	2.397(40)	1.8(1)	466(20)	657(60)	300(200)
A2$_{heptane}$	2.492(10)	2.25(20)	1.806(8)	393(20)	665(80)	380(20)

Figure S13. Experimental EPR spectra at T = 10 K of DUT-8(Ni$_{0.98}$Co$_{0.02}$) solvated in DCM (red), DMF (black) and n-heptane (blue).
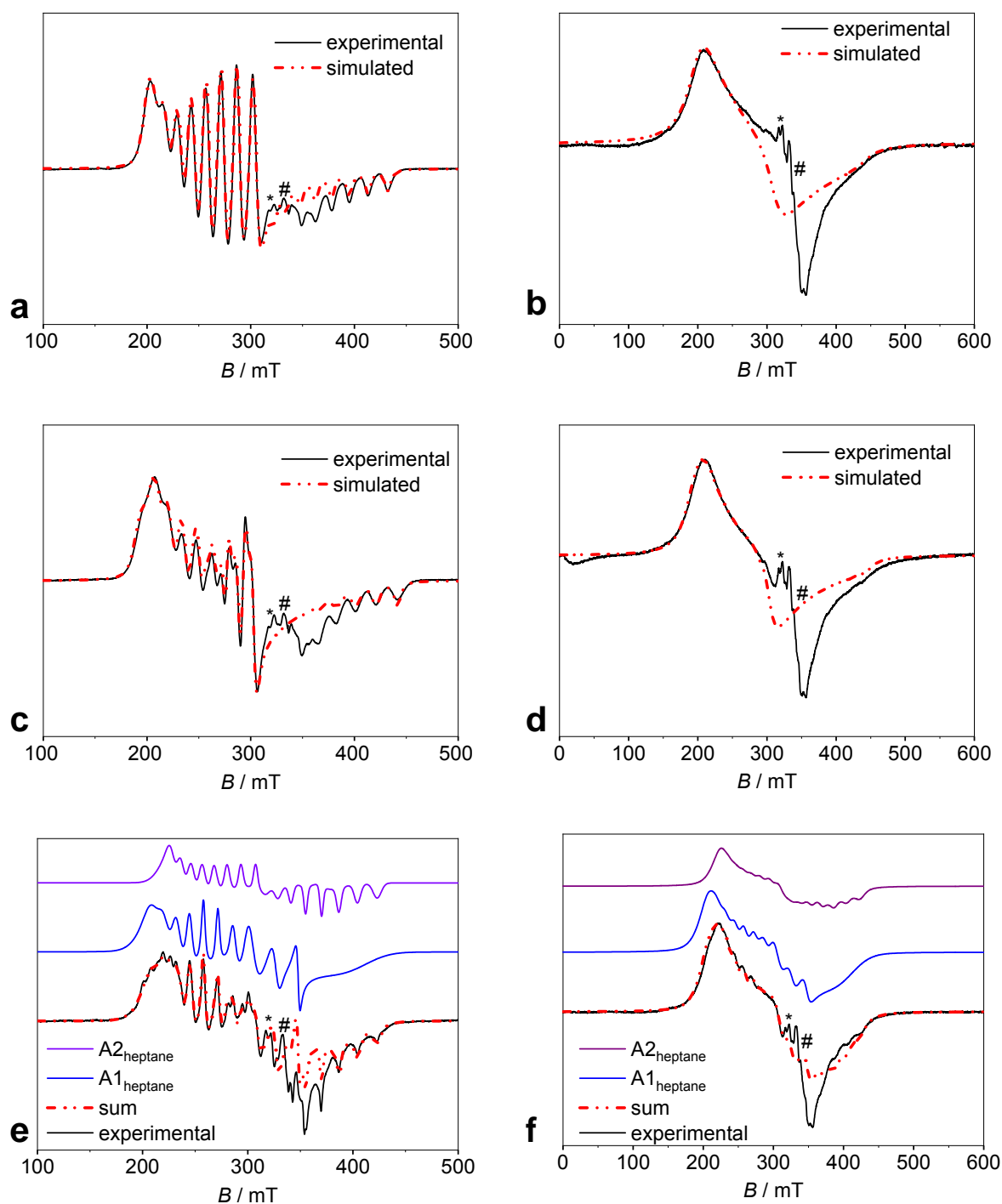
Figure S14. Experimental (black) and simulated (colored) EPR spectra of DUT-8($Ni_{0.98}Co_{0.02}$) solvated in DCM (**a,b**), DMF (**c,d**) and *n*-heptane (**e,f**). Spectra measured at T = 10 K (**a,c,e**) and T = 71 K (**b,d,f**) are shown. Spin Hamiltonian parameters used for the simulations are listed in table S4 and S5. For simulations at T = 10 K and T = 71 K almost all spin Hamiltonian and linewidth parameters are the same. Only the isotropic convolutional Lorentzian peak-to-peak linewidth was increased appropriately, when going from T = 10 K to T = 71 K. The red dotted lines in **e** and **f** are the sums of the simulated signals of species A1$_{heptane}$ and A2$_{heptane}$ shown above. The signal labeled with * might be assigned to some Ni^+, low spin Ni^{3+} or low spin Co^{2+} impurity or defect. The signal labeled with # might be assigned to some low spin Co^{2+} impurity or defect.

Assignment of the EPR signals. EPR spectra of samples DUT-8($Ni_{0.98}Co_{0.02}$) solvated in DCM, DMF and *n*-heptane measured at T = 10 K are shown in Figure S13. They show signals between 150 mT and 450 mT which exhibit a variety of lines. Their number suggests that they can be assigned to transitions split by the hyperfine interaction (*hfi*) with a ^{59}Co nucleus which has a nuclear spin I = 7/2. Corresponding octets of *hfi* transitions in the g-tensors x,y and z principal directions are marked in Figure S13 for the DCM solvated sample (assuming a co-alignment of the g- and ^{59}Co *hfi*-tensor). In fact, those signals can be assigned to effective electron spin S = 1/2 species interacting with a ^{59}Co nucleus. Respective EPR active species A_{DCM} and A_{DMF} were identified for the DCM and DMF solvated samples (see Table S4 for spin Hamiltonian parameters and Figure S14 for simulations). The EPR spectrum of the *n*-heptane solvated samples is more complicated and a unique assignment of the contributing paramagnetic species is intricate. However, our analysis suggests the contribution of at least two species $A1_{heptane}$ and $A2_{heptane}$ to the experimental spectrum and reasonable fits of the simulated to the experimental spectrum can be obtained with the g- and *hfi*-tensor principal values summarized in Table S5 (see Figure S14).

A more detailed assignment of the observed EPR active species requires further discussion. Since the observed signals show transitions characteristic of an effective spin S = 1/2 powder spectrum, we assign them to the lowest Kramer doublet of a half-integer electron spin species. We exclude the possibility that the observed signals originate from a monomeric *high spin* Co^{2+} (a $3d^7$ ion) with electron spin S = 3/2. Otherwise, the average effective g-value should be larger than $3.33^{19,20}$ whereas observed EPR active species in the present work have average g-values smaller than 2.4. We cannot fully exclude the assignment of the observed signals to monomeric *low spin* Co^{2+} ions (S = 1/2) as they might form as defective broken paddle-wheel units with one missing metal ion.[21] However, all signals show significant loss in spectral resolution at a temperature of T = 71 K as shown in Figure S14 whereas for *low spin* Co^{2+} species the spectral resolution is typically high up to temperatures of T = 130 K or above.[22-25] Such loss in spectral resolution at comparably low temperatures is rather typical for an electron species with a *high spin* Co^{2+} ion (S = 3/2) in distorted octahedral coordination where the coupling between the electron spin and the not fully quenched orbital momentum can shorten the spin lattice relaxation time significantly.[20,26] We therefore tentatively assign the observed EPR signals to dimeric mixed-metal Co^{2+}-Ni^{2+} paddle-wheel units of the open pore (*op*) phase in the respective solvated DUT-8($Ni_{0.98}Co_{0.02}$) samples. However, even with such an assignment different possible magnetic couplings have to be considered. The $3d^8$ Ni^{2+} ion in the mixed-metal paddle-wheel might be in an S = 0 ground state if the ligand field is sufficiently strong and low symmetric. For the same reason, the Co^{2+} might be in an S = 1/2 ground state explaining the observed EPR signals. In that case, one might again expect a higher spectral resolution at T = 71 K than we have observed (Figure S14) as discussed above when we considered an assignment to a monomeric *low spin* Co^{2+}. Furthermore, in a previous study of Cu^{2+} doped DUT-8($Ni_{0.98}Cu_{0.02}$) we have shown that the Ni^{2+} ion in the Ni^{2+}-Cu^{2+} paddle-wheel stays in an S = 1 *high spin* state.[27] Since it is reasonable that the strength and symmetry of the ligand field at the Ni^{2+} ion in the mixed-metal paddle-wheel does not change drastically if one exchanges the neighboring Cu^{2+} by a Co^{2+} ion, we expect that the Ni^{2+} ion in mixed-metal Ni^{2+}-Co^{2+} paddle-wheel units of the *op* phase is also in an S = 1 *high spin* state.

If the Co^{2+} ion is still in its *low spin* state, the magnetic coupling to the S = 1 spin of the Ni^{2+} can be described by a spin Hamiltonian

$$\hat{H} = \hat{H}_{Co} + \hat{H}_{Ni} + \hat{H}_{Ni-Co}.$$

Here, $\hat{H}_{Co}$ and $\hat{H}_{Ni}$ are the spin Hamiltonians of the isolated monomeric Co^{2+} and Ni^{2+} ions and the term $\hat{H}_{Ni-Co}$ contains all spin-spin interactions between both ions including the spin dipolar and exchange interaction. A sufficiently large isotropic exchange interaction[28] between both ions (*low spin* Co^{2+} and *high spin* Ni^{2+}) splits the magnetic states described by the Hamiltonian $\hat{H}$ into two submanifolds with effective spins S_{low} = 1/2 and S_{high} = 3/2. If the coupling between both ions is antiferromagnetic, the former is lowest in energy. In this case, it can be effectively described by a Hamiltonian $\hat{H}_{S_{low}}$ which includes a ^{59}Co *hfi* which is three times smaller than described by the monomeric spin Hamiltonian $\hat{H}_{Co}$.[28] Since the ^{59}Co *hfi* of monomeric *low spin* Co^{2+} is typically smaller than 1000 MHz[22,25,29,30], the ^{59}Co *hfi* parameters determined in the present work (Table S4 and S5) are far too large for an assignment to a mixed-metal paddle-wheel unit where a *low spin* Co^{2+} couples antiferromagnetically to a *high spin* Ni^{2+}, in case the isotropic exchange interaction is sufficiently large.

We can further exclude that the observed EPR signals can be described by the spin Hamiltonian $\hat{H}_{S_{\text{high}}}$ of the ground state submanifold if the S_{high} = 3/2 spin lies lowest in energy according to a ferromagnetic coupling between the *low spin* Co^{2+} and *high spin* Ni^{2+}. Otherwise, at least one effective g-tensor principal value should be larger than four.[31] As a conclusion, we suggest that the EPR active species A_{DCM}, A_{DMF}, $A1_{\text{heptane}}$ and $A2_{\text{heptane}}$ contributing to the EPR signals shown in Figures S13 and S14 can be assigned to mixed-metal Ni^{2+}-Co^{2+} paddle-wheel units. Here a *high spin S* = 3/2 Co^{2+} ion couples magnetically with a *high spin S* = 1 Ni^{2+} ion to form a state with a total effective electron spin S = 1/2. In general, such an interaction cannot be described by a simple spin Hamiltonian since the ground state of the Co^{2+} might be orbitally degenerated with significant contributions of unquenched orbital momentum to the magnetism of this species.[31-33] Accordingly, a more detailed characterization of the magnetic properties of those species goes beyond the scope of this work since it requires more knowledge about the monomeric spin Hamiltonians to pin down the increased number of magnetic parameters, uniquely.[31-33] Nevertheless, the effective g-tensor values observed in the present work are close to 2 which might indicate a magnetic coupling between the Ni^{2+} and Co^{2+} with significant contributions of antiferromagnetic exchange pathways as reported for Ni-Co pairs in dinuclear triketonate complexes.[31,32]

Solvent dependent characteristics of the EPR signals. We prepared EPR samples of DUT-8($Ni_{0.98}Co_{0.02}$) solvated in either DCM, DMF or *n*-heptane as explained in the experimental section of the supporting information. Their experimental EPR spectra are shown in Figures S13 and S14. All samples show at *T* = 10 K suspicious EPR signals between 150 mT and 450 mT. For reasons explained in the previous section, we tentatively assign those signals to mixed-metal Ni^{2+}-Co^{2+} paddle-wheel units of the open pore phase of this material. Spectral simulations show that only one species A_{DCM} contributes significantly to the experimental spectrum of the DCM solvated MOF as depicted in Figure S14a. In case of the DMF solvated sample only one species A_{DMF} contributes likewise to the experimental spectrum (Figure S14c). Their experimentally derived spin Hamiltonian parameters are summarized in Table S4. In case of the *n*-heptane solvated MOF, contributions of at least two magnetically different species lead to reasonable fits between the simulated and experimental EPR spectra as shown in Figure S14e) (see Table S5 for spin Hamiltonian parameters). However, we have to admit that due to the large number of resolved *hfi* transitions the determination of the spin Hamiltonian parameters is ambiguous.

The present EPR results allow some judgement about the symmetry of the mixed-metal paddle-wheel units in the samples. For species A_{DCM} the g- and *hfi*-tensors x and y principal values are close to each other, indicating a high degree of axial symmetry and suggesting that the corresponding paddle-wheel units have an almost fourfold rotational symmetry axis as expected for PW **a**. This is in line with the kind of superstructure containing a high fraction of D_{2d} loops assigned for the DCM solvated DUT-8(Ni) in this contribution. Only for the DCM solvent, our analysis suggests a high order of the 2,6-ndc ligand configuration with disorder parameters close to $\phi = 1$ and $\eta = 1$, where the 2,6-ndc coordination to each paddle-wheel obeys a C_4 symmetry axis (see Figures 2 and 3 in the manuscript and Figure S5b, S6). According to the results of the present work, for the DMF and *n*-heptane solvated samples the dominating 2,6-ndc coordination to the paddle-wheels obeys no fourfold symmetry axis as expected for PW **b**-**d** (Figure S5b). This correlates perfectly with the distinctly less symmetric g- and *hfi*-tensors derived for species A_{DMF} (Table S4), $A1_{\text{heptane}}$ and $A2_{\text{heptane}}$ (Table S5). For those species, the difference between the corresponding x and y principal values reflect the absence of any rotational axis with more than twofold symmetry in contrast to species A_{DCM}. Furthermore, the contributions of at least two species to the EPR signal of the *n*-heptane loaded sample might reflect the inhomogeneity among the 2,6-ndc coordination to the paddle-wheel units which is characteristic for the kind of disorder which we report in the present work.

References

1   Kavoosi, N. *et al.* Tailoring adsorption induced phase transitions in the pillared-layer type metal–organic framework DUT-8(Ni). *Dalton Trans.* **46**, 4685-4695 (2017).

2   Klein, N. *et al.* Monitoring adsorption-induced switching by [129]Xe NMR spectroscopy in a new metal–organic framework $Ni_2(2,6-ndc)_2(dabco)$. *Phys. Chem. Chem. Phys.* **12**, 11778-11784 (2010).

3   Mueller, U. *et al.* The macromolecular crystallography beamlines at BESSY II of the Helmholtz-Zentrum Berlin: Current status and perspectives. *Eur. Phys. J. Plus* **130**, 141 (2015).

4   Kohl, H. & Reimer, L. *Transmission electron microscopy: physics of image formation* (Springer, 2008).

5   O'Dell, L. A. & Schurko, R. W. QCPMG using adiabatic pulses for faster acquisition of ultra-wideline NMR spectra. *Chem. Phys. Lett.* **464**, 97-102 (2008).

6   Stoll, S. & Schweiger, A. EasySpin, a comprehensive software package for spectral simulation and analysis in EPR. *J. Magn. Reson.* **178**, 42-55 (2006).

7   Bon, V. *et al.* Exceptional adsorption-induced cluster and network deformation in the flexible metal–organic framework DUT-8(Ni) observed by in situ X-ray diffraction and EXAFS. *Phys. Chem. Chem. Phys.* **17**, 17471-17479 (2015).

8   Petkov, P. S. *et al.* Conformational isomerism controls collective flexibility in metal–organic framework DUT-8(Ni). *Phys. Chem. Chem. Phys.* **21**, 674-680 (2019).

9   Sheldrick, G. M. Crystal structure refinement with SHELXL. *Acta Cryst. C* **71**, 3-8 (2015).

10 Gerlach, M., Mueller, U. & Weiss, M. S. The MX beamlines BL14. 1-3 at BESSY II. *J. large-scale Res. Facil.* **2**, 47 (2016).

11 Sparta, K. M., Krug, M., Heinemann, U., Mueller, U. & Weiss, M. S. XDSAPP2. 0. *J. Appl. Cryst.* **49**, 1085-1092 (2016).

12 Sheldrick, G. CELL_NOW, version 2008/4. *Georg-August-Universitat Göttingen: Göttingen, Germany* (2008).

13 SAINT, V. 8.34 A. *Bruker AXS Inc.: Madison, WI* (2014).

14 Sheldrick, G. M. *TWINABS. Ver. 2012/1* (2012).

15 Nagle, J. Theory of the dielectric constant of ice. *Chem. Phys.* **43**, 317-328 (1979).

16 Barkema, G. & Newman, M. Monte Carlo simulation of ice models. *Phys. Rev. E* **57**, 1155 (1998).

17 Ehrling, S. *et al.* Crystal size versus paddle wheel deformability: selective gated adsorption transitions of the switchable metal-organic frameworks DUT-8(Co) and DUT-8(Ni). *J. Mater. Chem. A* **7**, 21459-21475 (2019).

18 Smallwood, I. *Handbook of organic solvent properties* (Butterworth-Heinemann, 2012).

19 Tinkham, M. Paramagnetic resonance in dilute iron group fluorides. II. Wave functions of the magnetic electrons. *Proc. R. Soc. Lond. A* **236**, 549-563 (1956).

20 Lässig, D., Lincke, J. r., Griebel, J., Kirmse, R. & Krautscheid, H. Synthesis, crystal structure, and electron paramagnetic resonance investigations of heteronuclear CoII/ZnII and CoII/CdII coordination polymers. *Inorg. Chem.* **50**, 213-219 (2011).

21 Friedländer, S. *et al.* Single crystal electron paramagnetic resonance with dielectric resonators of mononuclear Cu^{2+} ions in a metal–organic framework containing Cu_2 paddle wheel units. *J. Phys. Chem. C* **119**, 19171-19179 (2015).

22 Lubitz, W., Winscom, C., Diegruber, H. & Möseler, R. EPR characterisation of bis(dimethylglyoximato)-cobalt(II) complexes and their oxygen adducts synthesised in an X-Zeolite matrix. *Z. Naturforsch. A* **42**, 970-986 (1987).

23 Kirmse, R. & Beyer, L. ESR-Untersuchungen zu Struktur-und Bindungsverhältnissen von tri-und bicyclischen Cobalt (II)-und Kupfer (II)-Chelaten mehrzähniger Schiffscher Basen des

Typs M(ONNO) und M(SN)$_2$ sowie zur Sauerstoffadduktbildung der Cobalt(II) Chelate. *Z. Anorg. Allg. Chem.* **498**, 185-198 (1983).

24 Garcia–España, E. *et al.* Low-spin six-co-ordinate cobalt (II) complexes. A solution study of tris (violurato) cobaltate (II) ions. *Dalton Trans.*, 101-104 (1988).

25 van Doorslaer, S. *et al.* Axial solvent coordination in "base-fff" cob(II)alamin and related co(II)-corrinates revealed by 2D-EPR. *J. Am. Chem. Soc.* **125**, 5915–5927 (2003).

26 Zarembowitch, J. & Kahn, O. Magnetic properties of some spin-crossover, high-spin, and low-spin cobalt (II) complexes with Schiff bases derived from 3-formylsalicylic acid. *Inorg. Chem.* **23**, 589-593 (1984).

27 Mendt, M., Ehrling, S., Senkovska, I., Kaskel, S. & Pöppl, A. Synthesis and characterization of Cu-Ni mixed metal paddlewheels occurring in the metal-organic framework DUT-8(Ni$_{0.98}$Cu$_{0.02}$) for monitoring open-closed-pore phase transitions by X-Band continuous wave electron paramagnetic resonance spectroscopy. *Inorg. Chem.* **58**, 4561–4573 (2019).

28 Buluggiu, E. EPR study on Mn^{2+}-Cu^{2+} and Ni^{2+}-Cu^{2+} mixed pairs. *J. Phys. Chem. Solids* **41**, 1175–1180 (1980).

29 Hitchman, M. A. Electronic structure of low-spin cobalt(II) Schiff base complexes. *Inorg. Chem.* **16**, 1985–1993 (1977).

30 Vinck, E., van Doorslaer, S., Murphy, D. M. & Fallis, I. A. The electronic structure of N,N′-bis(3,5-di-tert-butylsalicylidene)-1,2-cyclohexane-diamino cobalt(II). *Chem. Phys. Lett.* **464**, 31–37 (2008).

31 Banci, L., Bencini, A., Benelli, C., Dei, A. & Gatteschi, D. ESR spectra of nickel(II)-copper(II) and nickel(II)-cobalt(II) exchange-coupled pairs in transition-metal dinuclear triketonate complexes. *Inorg. Chem.* **20**, 1399–1402 (1981).

32 Banci, L., Bencini, A., Benelli, C. & Gatteschi, D. Exchange interactions in heterodinuclear complexes with one ion possessing an orbitally degenerate ground state. Nickel(II)-cobalt(II) pairs in diaqua(1,4-dihydrazinophthalazine)nickel(II) chloride hydrate. *Inorg. Chem.* **21**, 3868–3872 (1982).

33 Kahn, O., Tola, P. & Coudanne, H. Exchange interaction and orbital degeneracy in the Cu(II)-Co(II) heterobinuclear complex. *Chem. Phys.* **42**, 355–361 (1979).